A hybrid, image-based and biomechanics-based registration approach to markerless intraoperative nodule localization during video-assisted thoracoscopic surgery

Pablo Alvarez, Simon Rouzé, Michael I Miga, Yohan Payan, Jean-Louis Dillenseger, Matthieu Chabanas

A hybrid, image-based and biomechanics-based registration approach to markerless intraoperative nodule localization during video-assisted thoracoscopic surgery

Pablo Alvarez[a,b], Simon Rouzé[a,c], Michael I. Miga[d], Yohan Payan[b], Jean-Louis Dillenseger[a,*], Matthieu Chabanas[b,d]

[a] *Univ. Rennes 1, Inserm, LTSI - UMR 1099, F-35000 Rennes, France*
[b] *Univ. Grenoble Alpes, CNRS, Grenoble INP, TIMC-IMAG, F-38000 Grenoble, France*
[c] *CHU Rennes, Department of Cardio-Thoracic and Vascular Surgery, F-35000 Rennes, France*
[d] *Vanderbilt Institute for Surgery and Engineering, Vanderbilt University, Nashville, TN, USA*

Abstract

The resection of small, low-dense or deep lung nodules during video-assisted thoracoscopic surgery (VATS) is surgically challenging. Nodule localization methods in clinical practice typically rely on the preoperative placement of markers, which may lead to clinical complications. We propose a markerless lung nodule localization framework for VATS based on a hybrid method combining intraoperative cone-beam CT (CBCT) imaging, free-form deformation image registration, and a poroelastic lung model with allowance for air evacuation. The difficult problem of estimating intraoperative lung deformations is decomposed into two more tractable sub-problems: (i) estimating the deformation due the change of patient pose from preoperative CT (supine) to intraoperative CBCT (lateral decubitus); and (ii) estimating the pneumothorax deformation, *i.e.* a collapse of the lung within the thoracic cage. We were able to demonstrate the feasibility of our localization framework with a retrospective validation study on 5 VATS clinical cases. Average initial errors in the range of 22 to 38 mm were reduced to the range of 4 to 14 mm, corresponding to an error correction in the range of 63 to 85%. To our knowledge, this is the first markerless lung deformation compensation method dedicated to VATS and validated on actual clinical data.

Keywords: Biomechanical modeling, Image registration, Lung deformation, Video-assisted thoracoscopic surgery

1. Introduction

Lung cancer is the leading cause of cancer death among both men and women, making up more than 18% of all cancer deaths (Bray et al., 2018). The high mortality of lung cancer is associated with its asymptomatic nature that hinders its early detection, diagnosis and treatment. However, the advent of screening programs with low-dose computed tomography (CT) have significantly increased patient survival (Henschke et al., 1999; National Lung Screening

*Corresponding author.
Email addresses:
pablo-arturo.alvarez@univ-rennes1.fr (Pablo Alvarez), simon.rouze@chu-rennes.fr (Simon Rouzé), michael.i.miga@vanderbilt.edu (Michael I. Miga), yohan.payan@univ-grenoble-alpes.fr (Yohan Payan), jean-louis.dillenseger@univ-rennes1.fr (Jean-Louis Dillenseger), matthieu.chabanas@univ-grenoble-alpes.fr (Matthieu Chabanas)

Trial Research Team et al., 2011). Surgical resection is considered one of the best curative treatments for patients with early-stage lung cancer. Historically, lung lobectomy (*i.e.* the removal of entire lung lobes) through open thoracotomy was the chosen protocol. Within the last decades, clinical practice has evolved towards less invasive, better tissue preserving techniques. For instance, minimally-invasive video-assisted thoracoscopic surgery (VATS) has proven to yield equivalent clinical outcomes while improving patient care, and decreasing both the length of hospitalization and post-operative complications (Falcoz et al., 2016). In parallel, the interest for smaller, non-anatomical resections (wedge resections) has arisen for small nodules as a substitute to lung lobectomy. Although no consensus has been reached yet, studies suggest that the use of appropriate negative margins during wedge resections could provide patient outcomes equivalent to those of traditional lobectomies (Mohiuddin et al., 2014; Wolf et al., 2017). However, this shift from lung lobectomy to wedge resection through minimally-invasive VATS has introduced new surgical challenges. For instance, thoracic incisions to insert surgical instrument break the pressure equilibrium in the intrapleural space and cause air to flow into the thoracic cage. This abnormal air inflow, known as a pneumothorax, induces very large tissue deformation by collapsing the lung. While this voluntary induced pneumothorax is required to create surgical workspace, it significantly impairs the intraoperative localization of lung nodules, especially for small nodules that are generally not visible to the naked eye nor palpable through thoracoscopic instruments (Chao et al., 2018). Failing to localize lung nodules during VATS may ultimately result in unplanned surgical conversion to open thoracotomy, with a conversion rate as high as 54% reported in some studies (Suzuki et al., 1999). Therefore, several nodule localization strategies are commonly used in clinical practice. The main approach consists in placing fiducial markers in the nodule to facilitate its intraoperative localization. This nodule marking generally requires an additional preoperative procedure, before surgery, for the placement of hookwires, microcoils, or dyes under fluoroscopy guidance (Keating and Singhal, 2016). Despite the high success rates reported for these nodule localization techniques (Chao et al., 2018), the risk of marker migration is still non negligible and the patient is subject to additional radiation exposure. Furthermore, the optimal coordination of the two procedures (*i.e.* preoperative localization and surgical resection) may become a logistic burden, while the patient is at risk during the transfer from the CT suite to the operating room.

To overcome the problems associated with preoperative localization procedures, intraoperative nodule localization has been proposed. This strategy relies on intraoperative imaging to guide nodule-marker placement immediately before surgery, generally in a hybrid operating room. For instance, Gill et al. (2015) have introduced the iVATS system that uses a C-arm to localize nodules placing metal fiducial markers under fluoroscopy guidance. Other groups have implemented similar approaches combining intraoperative CT guidance with either hookwire (Zhao et al., 2016), dye (Yang et al., 2016), or double nodule marking (Chao et al., 2019). Chao et al. (2018) showed that these intraoperative localization techniques were associated with decreased time at risk but increased time in the operating room, without any significant difference in clinical outcomes with respect to preoperative localization.

Another intraoperative localization paradigm consists in markerless approaches. The idea is to use intraoperative imaging on the patient under operating conditions, namely, after the insertion of surgical ports and the induction of pneumothorax. This allows to localize the nodule immediately before its surgical resection. Several authors have proposed to use intraoperative ultrasound for the localization of lung nodules (Kondo et al., 2009; Rocco et al., 2011; Wada et al., 2016). In these images, nodules can be identified as hyperechoic regions with hypoechoic shadows (Kondo et al., 2009). However, this strategy is highly expert-dependent and requires a fully deflated lung, which is in many cases unfeasible. Another method has been introduced by Rouzé et al. (2016) in a hybrid operating room. A Cone Beam CT (CBCT) image of the semi-deflated lung is used for the localization and delineation of the nodule. This delineation is then registered to intraoperative fluoroscopic images that are used for guidance. A clinical study per-

formed on 8 patients demonstrated the feasibility of this approach. While promising, all these intraoperative markerless approaches rely entirely on the nodule visibility in the images, which may be limited in many cases by the reduced quality and contrast of intraoperative images. For instance, the fuzzy borders and low-density of ground glass opacity (GGO) nodules could make them indistinguishable from normal parenchyma in a low-contrast CBCT or US image. To overcome this limitation, we believe that image registration techniques can be used to bring preoperative surgical planning information into the intraoperative setting.

Image registration has been previously used to compensate for lung deformation to improve the efficiency of medical lung imaging in the diagnosis, treatment-planning, and guided intervention of lung diseases (McClelland et al., 2013). Several registration methods have been proposed based on image intensity (Murphy et al., 2011), biomechanical models (Al-Mayah et al., 2010; Seyfi Noferest et al., 2018), or a combination of both (Han et al., 2017). The applicability of these methods is currently restricted to lung breathing motion, mainly for conformational radiation therapy. However, lung deformation is considerably larger during VATS (Alvarez et al., 2018) which increases the difficulty of the registration problem. To our knowledge, only a handful of works have addressed the problem of lung nodule localization during VATS through image registration (Alvarez et al., 2019a; Uneri et al., 2013; Lesage et al., 2020). This paper presents a novel method to address this problem, evaluated for the first time on actual VATS clinical cases.

The contributions of this work can be summarized as follows: (i) we propose a markerless approach for lung nodule localization during VATS that is based on intraoperative CBCT imaging and image registration techniques; (ii) we propose a hybrid registration method combining intensity-based and biomechanics-based image registration; (iii) we specifically take into account lung deformation resulting from the patient's change of pose, the pneumothorax, the diaphragm movements, and the hilum deformation during the surgical procedure; and (iv) we evaluate our method on 5 retrospective clinical cases of patients that underwent wedge resection through VATS.

The remaining of this document is organized as follows: Sec. 2 presents an overview of existing methods for lung deformation estimation. Sec. 3 provides an overview of our proposed approach. Sec. 4 describes the lung biomechanical model used, then Secs. 5, 6, and 7 describe the processing steps of our registration method. Results are reported in Sec. 8 and discussed in Sec. 9, and Sec. 10 provides final concluding remarks.

2. Related works

The lung is a very soft, highly deformable organ in constant deformation due to breathing, heart beats, and body movements. A wide variety of image registration techniques based on image intensity, biomechanical models, or hybrid approaches have been developed to compensate for such deformation. These techniques were proposed mainly in the context of breathing motion, with CT images typically acquired by pairs at the end of inhalation and exhalation, or during the entire breathing cycle through 4DCT. In this study, our interest is the compensation of lung deformation during VATS using intraoperative CBCT imaging. Breathing deformation and VATS deformation have different causes and orders of magnitude, the latter being significantly larger. During normal breathing, lung deformation results from the contraction and relaxation of respiratory muscles that induce volumetric changes. The lung parenchyma can slide against the thoracic cage thanks to the lubricating liquid that separates these structures. During VATS, lung deformation results mostly from a change of patient pose, the insertion of surgical ports, and the general anesthesia. The insertion of surgical ports induces a pneumothorax that deflates the lung parenchyma and deforms the hilum. General anesthesia also relaxes the diaphragm muscle that consequently moves towards the apex, pushed by the weight of abdominal organs. The combination of these factors with the reduced quality of intraoperative CBCT images make the compensation of lung deformation for nodule localization during VATS a real challenge.

2.1. Intensity-based image registration methods for lung deformation compensation

Besides large lung deformation, sliding motion against the thoracic cage is widely known to be one of the major challenges encountered when dealing with intensity-based elastic registration of the lung parenchyma. Anatomically, the deformation of the lung and surrounding structures are constrained at the interface in the normal direction, but move almost freely in the tangential direction. However, most transformation models used in medical image registration assume a continuous deformation field that can not model this sliding effect (Maintz and Viergever, 1998; Sotiras et al., 2012).

Several authors have introduced methods for taking into account sliding interfaces for lung registration. Anatomical segmentations can be used to independently register the structures at the interface (Rietzel and Chen, 2006). With this technique, classical image registration algorithms can be used with little or no modification. However, gaps or overlaps may appear at the interface as a result of the independent registration. One solution consists in using a boundary-matching penalty method so that the interfaces are tied together. Wu et al. (2008) proposed to dilate the segmentations after a masking procedure to enforce the alignment of the interface. Another strategy is based on decomposing the deformation field at the interface into normal and tangential components. Sliding motion can be preserved by applying regularization on the normal component (Schmidt-Richberg et al., 2012), or by using a composite transformation with a shared normal component but independent tangential components (Delmon et al., 2013). The main drawback of these methods is the need for anatomical segmentations. Indeed, these segmentations are time-consuming to extract manually or may be inaccurate if extracted automatically, especially for pathological lungs or low contrast images. To overcome this issue, other works have proposed methods without prior anatomical segmentations. Ruan et al. (2009) presented a regularization strategy that discriminates the divergence and the curl of the deformation field separately. Sliding motion is preserved by allowing large shearing while penalizing other forms of non-smooth deformation. Another technique consists in using several layers of supervoxels (*i.e.* groups of neighboring voxels with similar intensities) connected using minimum spanning trees (Heinrich et al., 2016). The deformation field is enforced to be smooth across edge connections via regularization. However, non-connected supervoxels are allowed to be registered independently, hence preserving sliding motion.

In a previous preliminary study, we applied the method proposed by Wu et al. (2008) to register two intraoperative CBCT images of the undeformed and deformed lung acquired during a VATS intervention (Alvarez et al., 2019b). We managed to obtain reasonable alignment of the lung surface, but insufficient alignment of the internal structures. To our knowledge, no other study has addressed the same problem using intensity-based image registration only.

2.2. Biomechanical model-based methods for lung deformation compensation

Another approach for lung deformation compensation is the use of biomechanical models describing the lung's behavior. The Finite Element Method (FEM) is commonly used to obtain numerical solutions to the underlying equations. For instance, Zhang et al. (2004) proposed a Finite Element (FE) deformable model of the lung reconstructed at the end of exhalation to simulate lung expansion motion. The thoracic cage surface at the end of inhalation was included in the formulation as frictionless contact conditions that constrained lung expansion. A uniformly distributed negative surface pressure was applied to the deformable model until it filled the thoracic cage. A similar approach to lung expansion motion was proposed by Werner et al. (2009). The authors performed a study on 12 lung tumor patients and evaluated how changing tissue parameters affect the estimated deformations. The results suggested that if tissue homogeneity was considered, changing tissue parameters could only produce marginal perturbations in lung deformation, since it was mainly dictated by the limiting geometry of the thoracic cage. Another study investigated the effect of tissue heterogeneity while modeling lung expansion (Ilegbusi et al., 2014). The elasticity modulus was estimated

locally using an inverse non-invasive method. In average, the obtained values decreased with proximity to the diaphragm. The authors showed that the history of deformation as well as its spatial distribution were different when considering heterogeneous versus homogeneous material properties. Other authors have also investigated the use of non-constant, non-uniformly distributed negative surface pressures to produce lung expansion. Eom et al. (2010) computed negative pressure values from patient-specific Pressure-Volume (P-V) curves calculated from 4DCT data. The FE deformation predictions for the whole breathing cycle were more accurate than simple linear interpolation between end expiration and end inspiration deformations. Fuerst et al. (2015) automatically divided the lung surface in disjoint contact zones. The negative pressure applied at the surface was then differentiated for each contact zone, the specific values being found through an inverse problem formulation. Although the authors used homogeneous material properties, the results suggested an improvement of the deformation estimation thanks to the heterogeneous surface pressures.

Several works have also approached lung deformation estimation during breathing as a contraction motion. Al-Mayah et al. (2008) proposed a deformable model of the lung and surrounding structures reconstructed at the end of inhalation. Surface displacements from the end inhalation to the end exhalation phases were found using a mesh morphing method. These displacements were imposed as boundary conditions on the inner surface of the thoracic cage, which is in direct contact with the deformable lung model. Interactions between the lung and thoracic cage were modeled via frictionless contact, which allowed the integration of lung sliding. This study was further extended to investigate the effects of contact friction (Al-Mayah et al., 2009) or heterogeneous material properties (Al-Mayah et al., 2010), as well as the influence of linear and non-linear elasticity constitutive laws (Al-Mayah et al., 2011).

All the methods reported above model the lung parenchyma as a single elastic continuum. In reality, the volume occupied by the lung is composed of not only the parenchyma but also a great quantity of air stored inside the airways and alveoli. External forces exerted by the respiratory muscles allow the inhalation or exhalation of air from the lung, ultimately resulting in tissue deformation. Following this interpretation, the lung can be modeled as a porous medium composed of two coexisting physical domains: a solid domain (*i.e.* the parenchyma) and a fluid domain (*i.e.* the air flowing inside the lung). Physical laws governing the behavior of such porous medium constitute the theory of poroelasticity, which has been previously used to model breathing deformation. For instance, Ilegbusi et al. (2012) proposed a poroelastic model to simulate lung deformation for a complete breathing cycle. Boundary conditions for the fluid and solid domains consisted in a time varying positive pressure and a fixed support, respectively. The authors reported realistic deformations including a hysteresis deformation effect when accounting for heterogeneous material properties. Gravity was later added in the loads which improved the accuracy of the predicted deformation (Seyfi Noferest et al., 2018). Berger et al. (2016) also proposed a dynamic poroelastic model of the lung tightly coupled with an airway network modeling the airways. Physiologically realistic global measurements were reported for normal and physiological breathing, using varying airflow resistance and local elasticity.

To our knowledge, a single study has been very recently proposed by Lesage et al. (2020) to simulate lung deflation during a pneumothorax. A hyperelastic model is constrained by external pressure, reducing the model volume until matching the observed deflated lung volume. However, two CT images of the whole lung in supine position are used in this study which provides much more information than what can be available during VATS. In terms of modeling, a limit could be to estimate the deformation by large tissue strain only while the loss of air can be preeminent for a pneumothorax during VATS. A poroelastic model could instead be better suited to separate the deformation of the two different media, to model the air-tissue coupling in a macro-scale and cost-effective manner, as well as to simulate air loss from the fluid domain.

2.3. Hybrid methods for lung deformation compensation

Both image intensity-based and biomechanical-based methods have advantages and disadvantages. Intensity-based methods are limited by the intrinsic quality of intraoperative images and the need for complex regularization strategies for realistic motion estimation. On the other hand, good results can be obtained on a voxel-by-voxel basis, especially for internal structures, provided that images of adequate quality are available. Biomechanical models are limited by the uncertainties in boundary conditions needed for realistic lung motion simulations, the large variability in tissue parameters that could be difficult to estimate accurately, or the compliance of their computational needs with clinical practice. However, when compared with intensity-based methods, biomechanical models can work with less data as the underlying biophysical representation naturally constrains the solution space. In addition, these models are boundary-valued problems, which are compatible with environments where primarily only surface information is available. Also, approaches that use modeled physical and physiological phenomena may provide insight into understanding disease and its effects on lung behavior. The hypothesis of hybrid methods is that combining the two strategies allows to compensate for their individual limitations.

Hybrid methods have already been investigated for lung deformation estimation. Li et al. (2008) used intensity-based image registration to estimate a deformation field from end of exhalation to end of inhalation breathing phases. Dirichlet boundary conditions (*i.e.* imposed displacements) were then computed by interpolating the deformation field on the surface nodes of a deformable FE lung mesh. A similar approach was employed by Tehrani et al. (2015), who used Demons image registration to estimate surface displacement boundary conditions at several moments of the breathing cycle. In addition, the authors studied the effects of tissue parameters and non-linear elasticity laws on tumor displacement estimation accuracy, reporting best results under non-linear elasticity assumptions.

Other studies have used intensity-based image registration to reduce residual errors resulting from biomechanical model motion estimation. For example, Samavati et al. (2015) used a elasticity lung model to estimate lung contraction between end of inhalation and end of exhalation. The estimated deformation was then refined using intensity-based registration, which improved their estimation accuracy. Han et al. (2017) applied the same methodology to lung expansion deformation estimation during breathing. The authors compared their approach to only intensity-based or only biomechanical-model based registration, and also evaluated the influence of tissue parameters, contact friction and tissue heterogeneity. Their results show a better performance of the hybrid approach, similar to that of intensity-based approaches that account for sliding motion. The uncertainty of model parameters was accounted for by the refinement image-intensity step, allowing the use of simplified assumptions for the biomechanical models in hybrid approaches.

Finally, Uneri et al. (2013) carried out a preliminary study using CBCT images of an inflated and deflated ex-vivo pig lung. Although the authors did not use biomechanical modeling, a hybrid approach was implemented combining surface morphing and nonrigid intensity-based image registration. The reported results were promising, but the applicability of their method to clinical practice remains to be determined, since the quality of intraoperative VATS images is potentially lower than that of the images used by the authors. Nakao et al. (2019) proposed a surface-based shape model of lung deflation validated on Beagle lungs, and more recently incorporated manually placed landmarks to help with their estimation (Maekawa et al., 2020). However, validation results were reported only for surface landmarks, and the applicability to internal lung deformation remains to be investigated. To our knowledge, these are to date the only studies within the VATS context, but are limited to animal specimens in non-clinical conditions.

In a preliminary study, we recently proposed a hybrid approach to account for pneumothorax related lung deformations (Alvarez et al., 2019a). This method was evaluated on a retrospective clinical case of needle biopsy with pneumothorax complication, using a preoperative CT of the inflated lung and a

postoperative low-dose CT of the deflated lung. The present work complements our deformation compensation approach and propose its adaption to actual intraoperative CBCT images acquired during VATS interventions.

3. Method Overview

From the preoperative, routinely acquired structural chest CT image to the intraoperative surgical conditions, the lung undergoes very large deformation. This deformation may be understood as a combination of two main factors: (i) a change of the patient pose from supine to *lateral decubitus*, which changes the orientation of the body and hence the influence of gravity on internal structures; and (ii) the pneumothorax, which induces lung and hilum deformation. Accounting for these two sources of deformation at once is a nontrivial task. To reduce the complexity of this challenge, we thus introduced a functional approach that treats each source of deformation independently in two sequential phases. The lung deformation caused by the change of patient pose was first estimated, followed by the one resulting from the pneumothorax. Intraoperative CBCT images at each phase provided structural information of the deformed lung, which was integrated into our hybrid nonrigid registration framework. In total, three anatomical images were used in this study: a preoperative CT image containing the whole lung of the patient in supine position (CT), and two intraoperative CBCT images of the patient in *lateral decubitus* position. The CBCT images provide a partial view of the inflated lung before pneumothorax (CBCT_{inf}) and the deflated lung after pneumothorax (CBCT_{def}), respectively. It should be noted that only the CT image is used in the clinical protocol of a VATS intervention. Figure 1 shows the three images for one clinical case.

The overall methodology proposed in this work is depicted in Fig. 2. A patient-specific biomechanical lung model was first built from the preoperative CT image. As a first approximation, we considered the lung as a single unified structure. The three or two lobes of a right or left lung, respectively, were then not modeled separately. A poroelastic constitutive

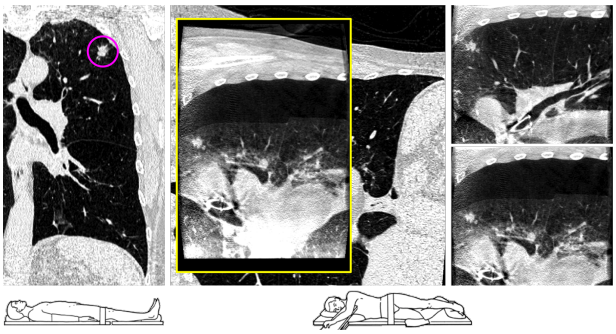

Figure 1: Left: preoperative CT image with the patient in supine position. Right: intraoperative CBCT images of the inflated (CBCT_{inf}) and deflated (CBCT_{def}) lung with the patient in *lateral decubitus* position. Middle: superposition of the preoperative CT image rigidly registered to the intraoperative CBCT_{def} image. The FOV of the CBCT_{def} image (outlined in yellow) only provides a partial view of the lung. The nodule is encircled in the preoperative CT image and is visible in all other images.

law was chosen to represent the parenchyma and the air flow within the lung.

The first stage of our process, later referred as *Phase 1*, estimates the deformation associated to the patient change of pose. Nonrigid intensity-based image registration was performed between the CT and CBCT_{inf} images to compute the deformation within the field of view (FOV) of the CBCT_{inf} image. The biomechanical model was then used extrapolate this deformation to the whole extent of the lung, including portions that are not visible in CBCT_{inf}. This estimation of the whole lung geometry will allow defining proper boundary conditions in the next phase, which would not be possible with only the lung portion included in the CBCT_{inf} FOV. After this *Phase 1*, that will be detailed in Sec. 6, the complete intraoperative lung geometry before pneumothorax is thus estimated.

The second stage of our method, *Phase 2*, estimates the deformation induced by the pneumothorax. Surface information of the deflated lung was first extracted from the CBCT_{def} image, while also evaluating the associated deformation of the hilum. An inverse problem was then iteratively solved, using biomechanical simulations, to identify the model parameters that minimize a distance between the lung

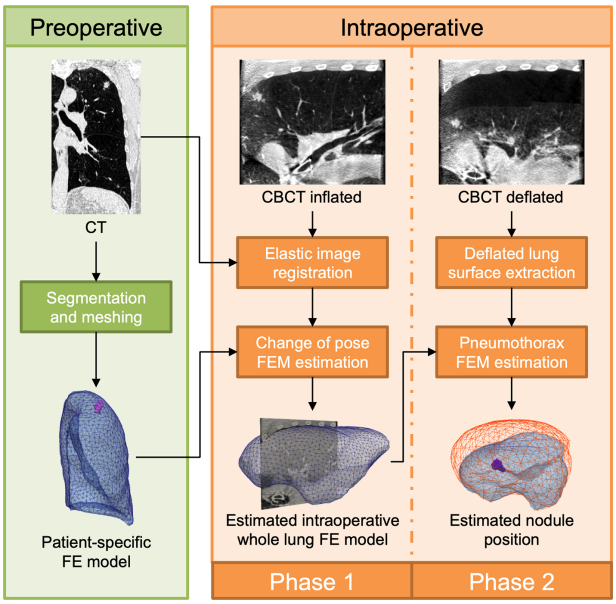

Figure 2: Overview of the proposed nodule localization framework. The process is split into two stages, *Phase 1* and *Phase 2*, that respectively estimate the change of pose deformation then the pneumothorax deformation.

model and the CBCT$_{def}$inputs. At the end of this process the final pneumothorax deformation is applied to the preoperative CT image, which provides an estimation of the intraoperative lung nodule position. *Phase 2* of our methodology will be described in Sec. 7.

4. Poroelastic model of the lung

The physical laws governing the poroelastic material used in this work were first introduced in Biot's theory of 3D soil consolidation (Biot, 1941, 1955). The total stress in the porous material is carried partly by the fluid and partly by the solid structure. The hydrostatic pressure of the fluid inside the pores generates tensile/compressive stresses that cause deformation of the whole medium. It is assumed that the total stress on the porous medium can be decomposed as the sum of the stress carried by the solid structure and the stress carried by the fluid (Verruijt, 2013). This is known as the principle of effective stress and is described by the expression

$$\boldsymbol{\sigma}_t = \boldsymbol{\sigma}_e - \alpha p \boldsymbol{I} \tag{1}$$

where $\boldsymbol{\sigma}_t$ and $\boldsymbol{\sigma}_e$ are the stress tensors for the total and effective stresses, p is the hydrostatic pore pressure and $\boldsymbol{I}$ is the second-order identity tensor. The parameter α is the Biot-Willis coefficient that describes the amount of bulk volume change that is explained by a pore pressure change under constant stress.

The definition of the effective stress tensor $\boldsymbol{\sigma}_e$ depends upon the mechanical behavior assumed for the solid medium. In this work, we used a first order approximation and adopted the theory of linear elasticity. We hypothesized that most of the deformation is caused by the fluid medium, thus, the solid medium was assumed linearly elastic (*i.e.* undergoing small deformation). The solid medium was also considered isotropic. It should be noted that more elaborate fluid-solid interaction non-linear models are possible and this work represents a linearization of considerably complex physics as a first step in understanding the potential of a model-based approach. Following these assumptions, the effective stress $\boldsymbol{\sigma}_e$ is related to the deformation tensor $\boldsymbol{\varepsilon}$ by the Hooke's constitutive equation

$$\boldsymbol{\sigma}_e = \lambda \; tr(\boldsymbol{\varepsilon}) \boldsymbol{I} + 2\mu \boldsymbol{\varepsilon} \tag{2}$$

where λ and μ are the Lamé constants that characterize the tissue's response to stress. These Lamé constants can also be written in terms of the Young's Modulus E and Poisson's ratio ν through the relations

$$\lambda = \frac{E\nu}{(1+\nu)(1-2\nu)} \qquad \mu = \frac{E}{2(1+\nu)} \tag{3}$$

The strain tensor $\boldsymbol{\varepsilon}$ of Eq. (2) is defined in terms of tissue displacements $\boldsymbol{u}$ as

$$\boldsymbol{\varepsilon} = \frac{1}{2}(\nabla \boldsymbol{u} + \nabla \boldsymbol{u}^T) \tag{4}$$

This corresponds to the definition of the infinitesimal strain tensor, where second-order terms are neglected. This is a first-order geometrical approximation of tissue deformation.

Mechanical equilibrium is reached when stresses within the porous medium are in balance with external loads. If inertial forces are not considered and the only external force is gravity, the total stress tensor $\boldsymbol{\sigma}_t$ must then satisfy the equilibrium equation

$$\nabla \cdot \boldsymbol{\sigma}_t + \rho \boldsymbol{g} = \mathbf{0} \tag{5}$$

where ρ is the density of the porous medium and $\boldsymbol{g}$ is the gravitational acceleration vector. Since the porous medium is composed of two phases, its density may also be defined in terms of its constituent densities as

$$\rho = \rho_s(1 - \phi) + \rho_f \, \phi \tag{6}$$

where ρ_s and ρ_f are the densities of the solid and fluid media, respectively, and ϕ is the porosity of the whole medium.

An additional equation is needed in order to complete the description of the continuum. In Biot's theory of consolidation, the fluid flows through the pores according to Darcy's law. This law proposes a relationship between the instantaneous flow rate $\boldsymbol{q}$ of an incompressible fluid through a porous medium, which is expressed by the equation

$$\boldsymbol{q} = -\frac{\kappa}{\mu_f} \nabla p \tag{7}$$

where κ is the intrinsic permeability of the porous medium and μ_f the dynamic viscosity of the fluid. The conservation of fluid and solid mass is expressed by the storage equation

$$\nabla \cdot \boldsymbol{q} + S \frac{\partial p}{\partial t} = -\alpha \frac{\partial \epsilon}{\partial t} \tag{8}$$

where S is the storativity parameter and $\epsilon = \partial u_x/\partial x + \partial u_y/\partial y + \partial u_z/\partial z = \nabla \cdot \boldsymbol{u}$ is the volumetric strain.

The term to the right hand of Eq. (8) expresses the time rate of change of dilatation/contraction of the solid matrix and how that affects the nature of fluid mass transport. For instance, if we consider the pores to be totally saturated with fluid, a negative rate of volumetric strain will shrink the porous material and immediately squeeze fluid out of the pores by means of raising interstitial pressure. Such fully saturated porous medium is modeled by choosing the parameters $\alpha = 1$ and $S = 0$. On the contrary, if the pores are not fully saturated with fluid, the rate of volumetric strain does not have an instantaneous effect on the distribution of pore pressure. This is represented by the second term of Eq. (8) being nonzero, which results in a delay on the transferal of volumetric strain to net fluid flow. The storativity parameter S is also understood as the amount of fluid that can be forced into the porous medium while maintaining a constant bulk volume. Eq. (8) is in essence a mass conservation law that relates changes in volumetric strain of the solid medium to changes in hydration level.

Animal studies were carried out by Miga et al. in order to evaluate the applicability of a poroelastic model to brain shift deformation compensation. The authors extracted *in vivo* measurements of displacement and interstitial pressure of interstitial fluid within the context of two separate deformations sources, an expanding mass represented by a balloon catheter (Paulsen et al., 1999), and a temporal piston-delivery system (Miga et al., 2000). The objective was to determine the accuracy of the poroelastic model to compensate for the main bulk brain deformation under surgically realistic loads. The results reported in those studies in conjunction with more recent follow-up studies (Narasimhan et al., 2018) suggest that deformation and interstitial pressure gradients measured from tissue can be predicted reasonably well using relatively simple boundary conditions on the poroelastic model. Another finding in the human environment was that sources of brain deformation were identified that involved significant fluid exchange with the parenchymal space as a result of hyperosmotic agents (Chen et al., 2011). This exchange is very similar to the evacuation of air occurring in the collapsing lung. Based on that work, an additional source term was incorporated into Eq. (8) to represent this fluid evacuation dynamic, so that the storage equation is rewritten as

$$\nabla \cdot \boldsymbol{q} + S \frac{\partial p}{\partial t} = -\alpha \frac{\partial \epsilon}{\partial t} - \kappa_b (p - p_c) \tag{9}$$

with $-\kappa_b(p - p_c)$ being the source term allowing for fluid evacuation. The parameter κ_b represents in-

trabronchi permeability. The parameter p_c represents the pressure at the interior of the anatomical structures that allow fluid evacuation. In this present work, p_c corresponds to intrabronchi pressure. It can be seen from Eq. (9) that fluid evacuation (*i.e.* fluid sinking) occurs for positive values of $\kappa_b(p - p_c)$. This modified version of the poroelastic equations was used to estimate brain shift deformation (Dumpuri et al., 2007; Kay Sun et al., 2014), and more recently yielded promising results to estimate lung pneumothorax deformation (Alvarez et al., 2019a).

Finally, Eqs. (5) and (9) fully describe the dynamic behaviour of a poroelastic material with allowance for fluid evacuation. However, computing the transition from the undeformed configuration to the equilibrium configuration is not necessary in our context. Instead, we only seek to estimate the deformation once the lung has settled after the pneumothorax. Consequently, computing only the equilibrium configuration is sufficient. We then implemented the steady-state version of the poroelastic equations previously presented, simplified as:

$$\nabla \cdot \boldsymbol{\sigma}_e - \alpha \nabla p + \rho \boldsymbol{g} = \mathbf{0} \qquad (10)$$

$$-\nabla \cdot \left(\frac{\kappa}{\mu_f} \nabla p \right) + \kappa_b (p - p_c) = 0 \qquad (11)$$

The solution to these equations was computed using a FEM formulation implemented on the open source library *GetFEM* (`http://getfem.org/`). The tissue parameters and boundary conditions used for each simulation are described in Sec. 7.2.

5. Preprocessing of the CBCT images

CBCT scanners produce image reconstruction artifacts as any other conventional CT scanner. However, the acquisition of the CT and CBCT images differ on the projection data used, namely 1D for the CT (fan-beam) and 2D for the CBCT (cone beam). The 2D projection strategy relies on larger detectors that allow the CBCT scanner to have a better spatial resolution and reduced irradiation dose (Kalender and Kyriakou, 2007). These are desirable features that make the CBCT scanner portable and OR-compatible. However, the benefits come in detriment of the image quality, since the larger detector suffers from higher image intensity scattering (Schulze et al., 2011), and the particular mechanics of the acquisition process introduce cupping, aliasing and truncation artifacts (Kalender and Kyriakou, 2007; Schulze et al., 2011). The presence of these artifacts will undermine the performance of any processing algorithm based on Hounsfield unit (HU) values. We thus proposed to pre-process CBCT images before applying our registration method.

Two artifacts affect HU values: the truncation artifact that appears when the imaged object is larger than the scanner FOV (Lehr, 1983), and the cupping artifact due to scatter radiation. As a result, the reconstructed images present an overestimation of HU values near the circular border of the FOV and an underestimation of HU values towards the center of the FOV. In this work, we assumed the reconstructed image to be the sum of real HU values and artifact effects. We modeled these artifact effects via a piecewise linear function that is circular symmetric with respect to the cranio-caudal axis (*i.e.* the rotation axis of the CBCT scanner) and constant across axial slices. The shape of this function was designed empirically by observing CBCT images. The artifact-corrected images were obtained by subtracting the modeled artifacts to the reconstructed images.

In addition to HU artifacts, reconstruction errors are also present at the superior and inferior borders of the FOV, in the cranio-caudal direction. These errors are caused by projection data missing in several projections of the whole gantry rotation, as well as beam scattering and aliasing. As a consequence, the reconstructed image is severely distorted in these regions, where structural information is almost completely lost. We observed that this effect is present in the axial slices of the first and last 12 mm of the image approximately. For all the processing algorithms described in subsequent sections, we did not take into account the information contained in these slices.

6. Phase 1: Estimation of the change of pose deformation

This section describes the *Phase 1* processes of the general workflow presented in Fig. 2. The aim is to

estimate the complete geometry of the lung in intraoperative conditions from the CBCT$_{inf}$ image, before the pneumothorax is induced. A schema of these *Phase 1* processes is presented in Fig. 3.

First, a deformation field was computed between the preoperative CT and intraoperative CBCT$_{inf}$ images via intensity-based image registration. The computed deformation field then defined imposed displacement boundary conditions for a biomechanical model, to extrapolate the deformation to the entire lung.

6.1. Image-based change of pose estimation

The intensity-based change of pose estimation consists in an initial rigid registration of the spine followed by a sub-anatomical elastic registration approach as proposed by Wu et al. (2008). This approach independently registers sliding structures by selectively masking image intensities with anatomical segmentations. Thus, a segmentation of lung parenchyma is necessary for each image. While this can be performed automatically in the CT image, it is much more challenging in the CBCT$_{inf}$ image due to artifacts, noise, and lung deformation after the change of pose.

Therefore, a multi-step method was implemented as follows: (i) alignment using rigid registration over the spine; (ii) lung segmentation in the CT image; (iii) initial elastic registration with the CT lung segmentation; (iv) lung segmentation of the CBCT image using the obtained deformation field, followed by a sub-anatomical elastic registration with both segmentations. The three registration processes were performed with the Elastix toolbox (Klein et al., 2010).

6.1.1. Rigid registration of the spine

The CT and CBCT$_{inf}$ images are defined in non-overlapping reference frames, as they were acquired by distinct scanners with the patient in a different pose. An initial rigid transformation between the two images is thus necessary before considering any local deformations. In this study, we used the spine for the rigid registration process, as it is the only structure that remains relatively rigid between the two images. Only small changes of curvature were observed, which were later captured with the elastic registration steps.

The spine was semi-automatically segmented in the CBCT$_{inf}$ image. First, a line profile crossing the spine was computed. Then, a minimal Region of Interest (ROI) containing the whole spine was determined using the spatial derivative of intensities on the line profile. After thresholding the image intensities within the ROI, connected component analysis and morphological operations yielded the final spine segmentation.

The rigid registration process was carried out with the preoperative CT as the *moving* image and the intraoperative CBCT$_{inf}$ as the *fixed* image. A Normalized Correlation Coefficient (NCC) similarity metric was computed over a series of 2000 image points randomly pooled from the spine segmentation. Since vertebrae resemble significantly one another, one spine landmark was manually selected to initialize the transformation and avoid shifting in the spine's direction.

6.1.2. Segmentation of the lung parenchyma in the CT image

The lung parenchyma was segmented in the preoperative CT image using our customized version of Chest Imaging Platform (`https://chestimagingplatform.org/`), an open source library for image processing and analysis of chest CTs. First, Otsu's thresholding method was used to generate an initial segmentation containing both lungs and the airways. A point inside the trachea was then automatically detected using connected component analysis on an axial slice at 40 mm from the top of this segmentation. This point was used as the starting seed of a 3D region growing algorithm that segmented the trachea and the first airway branches. The resulting airways segmentation was removed from the initial segmentation, which allowed the separation of the lungs. The segmentation of the operated lung was manually adjusted to include areas that remained poorly-segmented, notably near the hilum. Finally, morphological closing was used to fill in the remaining holes and to smooth out any sharp contours. With respect to the original method in Chest Imaging Platform, our implementa-

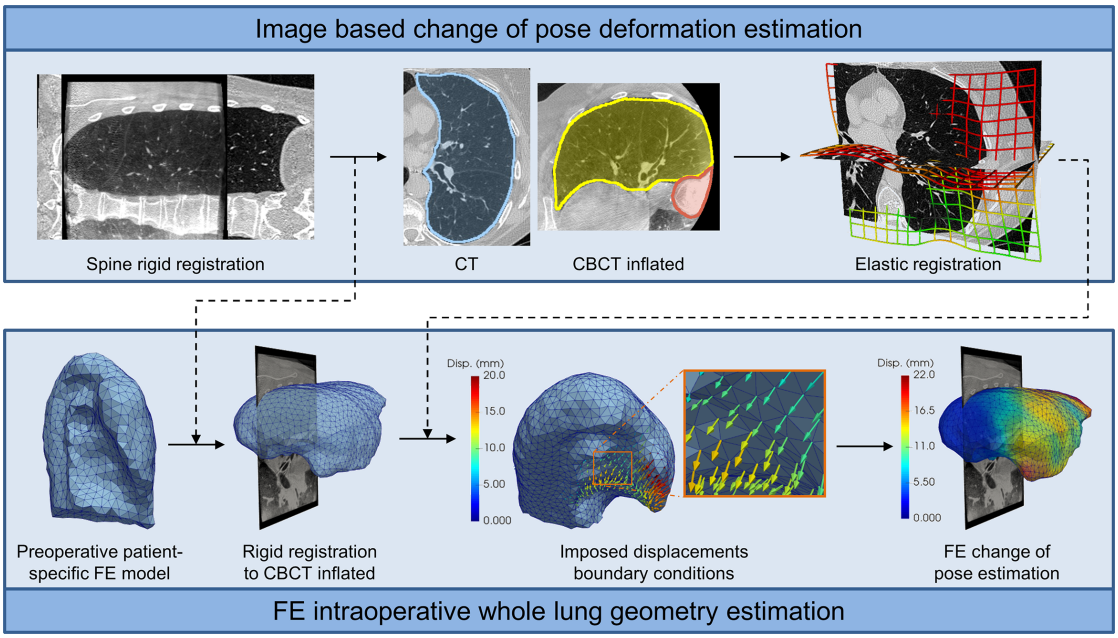

Figure 3: Schematic diagram of the *Phase 1* process to estimate the change of pose deformation. The top block illustrates the image-based registration of the preoperative CT and intraoperative CBCT_{inf} images. After rigidly registering the spine, an elastic registration based on anatomical segmentations of the lung is carried out. The bottom block concerns the estimation of the complete lung geometry after the change of pose deformation. The previously computed deformation field is transferred as imposed displacements boundary conditions on a FEM model. This model extrapolates the deformation to the whole extent of the lung, including regions that are not within the FOV of the CBCT_{inf} image.

tion detects automatically the seed point for the 3D region growing algorithm, and uses heuristics based on segmented volume ratios to avoid leakage during region growing.

6.1.3. Initial elastic registration

An initial elastic registration step was carried out, where the NCC similarity metric was computed from voxels inside the rigidly registered CT lung segmentation. Large deformations were accounted for using a multi-resolution Free Form Deformation (FFD) approach, with a B-Splines transformation model parameterized on a regular grid in the *fixed* image domain (*i.e.* CBCT_{inf}). A total of 5 incremental grid resolutions were used, with increments being computed by factors of two. The finest resolution had a regular grid size of 16 mm.

6.1.4. Sub-anatomical elastic registration

After the initial elastic registration, the CT lung segmentation was warped with the resulting deformation field to provide an estimation of the lung parenchyma segmentation in the CBCT_{inf} image. The resulting segmentation was manually adjusted to correct for poorly-segmented regions.

Finally, following Wu et al. (2008), both images were masked with the lung segmentations. Voxels outside the segmentations were replaced with a constant HU value below the range of possible parenchyma values (*i.e.* below -1000 HU, corresponding to air). The lung segmentation in the intraoperative CBCT_{inf} image was extended by 5 mm using morphological dilation, and elastic registration was performed again as described before (Sec. 6.1.3) but using the masked volumes and this extended segmentation. Using this approach, points lying outside the

lung in the *fixed* image are registered to the same intensity values in the *moving* image, which also lie outside the lung. In addition, matching outside points has no cost in terms of the similarity metric, which results in the registration process to be guided mostly by the information within the lung. As a result, this process minimizes the misalignment error of the internal lung structures while allowing sliding at the lung interface.

The resulting deformation field maps all points from the *fixed* image (CBCT_{inf}) domain to the *moving* image (rigidly registered CT) domain. Thanks to the multi-grid, multi-resolution transformation model, the spatial Jacobian of the deformation field is positive throughout the whole domain (Yongchoel Choi and Seungyong Lee, 1999). This ensures the invertibility of the deformation field, which was important to later compute imposed displacement boundary conditions.

6.2. Extrapolation of the deformation to the entire lung

The deformation field obtained in the previous step provides a first estimation of the change of pose deformation, but is limited to the FOV of the CBCT_{inf} image. A FEM model was then used to extrapolate this deformation to the entire lung, especially in the lung apex and/or the diaphragm area that are usually at least partially not visible.The hypothesis is that the unknown deformation in these regions can be estimated by means of mechanical forces that emerge to counter external loads applied in the middle of the lung (*i.e.* inside the FOV). In other words, deformation in unknown regions is estimated by finding a state of mechanical equilibrium after imposing the partially known deformation. Note that we did not try to simulate the very complex mechanisms of the patient change of pose; we have so far no means of estimating the actual external and body loads of this complex phenomenon. Instead, we tried to estimate the entire lung deformation for the practical purposes of intraoperative surgical guidance.

The following subsections describe the FE extrapolation process as illustrated at the bottom of Fig. 3.

6.2.1. FE mesh generation

The geometry of the lung was meshed from the preoperative lung segmentation using CGAL library (`https://www.cgal.org/`). This FE mesh consisted of approximately 27000 first order tetrahedral elements with an average size of 8 mm.

6.2.2. Computation of imposed displacements

The FEM boundary conditions were computed from the rigid transformation and the deformation field described previously in Sec. 6.1. First, the patient-specific preoperative FE mesh was rigidly registered to the intraoperative setting using the rigid transformation parameters. Then, we calculated the deformation associated to every node of the mesh lying within the bounds of the change of pose deformation field. The deformation field at every node position was inverted using the iterative algorithm proposed by Crum et al. (2007), to define the displacement from the rigidly registered CT domain to the CBCT_{inf} domain. As a result, we obtained a set of displacement vectors that can be used as nodal boundary conditions in a FE simulation. In the following, we will refer to these boundary conditions as imposed displacements.

6.2.3. FE estimation of the change of pose

The lung was modeled as a homogeneous and isotropic medium, governed by the laws described by Eqs. (10) and (11). We hypothesized that the change of pose deformation is mostly caused by gravity and contacts between the lung and its surrounding structures. Thus, effects of the fluid domain were assumed to be negligible at this stage, which implies fluid mass conservation with no flow throughout the whole domain.

For the fluid domain, we prescribed homogeneous Dirichlet boundary conditions of pressure at the whole lung surface, with the intrabronchi permeability parameter κ_b set to zero to ensure mass conservation. For the solid domain, imposed displacements were applied to surface and internal nodes using Dirichlet boundary conditions and Lagrange multipliers, respectively. The remaining nodes were left unconstrained.

Since imposed displacements boundary conditions enforce the final deformation, tissue parameters have little influence on the final equilibrium state. Thus, we simply used the parameters of the pneumothorax estimation phase described in Sec. 7.2.4.

7. Phase 2: Estimation of the pneumothorax deformation

This section describes the second stage of the general workflow presented in Fig. 2. The pneumothorax deformation was estimated using a pipeline based on an inverse formulation, as illustrated in Fig. 4. This inverse formulation fitted the lung biomechanical model to the real intraoperative deflated state observed in the CBCT_{def} image. The nodule position was then updated by warping the preoperative CT with the change of pose deformation and then the simulated pneumothorax deformation.

7.1. Intraoperative data processing

The intraoperative CBCT_{inf} and CBCT_{def} images can be in misalignment, because the patient may had to be moved between the two scans so that the surgeon could better perform the thoracic incisions. We thus rigidly registered these images using the spine as before (Sec. 6.1.1). The resulting transformation served to align the FE extrapolated lung model with the CBCT_{def} image. Afterwards, this image was processed to extract the surface of the deflated lung and to estimate the hilum deformation after pneumothorax.

7.1.1. Segmentation of the deflated lung surface

The lung deflation causes the complete collapse of some airway branches and alveoli. This condition, known as atelectasis, locally increases the density of the lung parenchyma, making its boundary with other soft tissues barely distinguishable in some regions. Therefore, automatically segmenting the deflated lung is extremely challenging. Since providing an automatic method was out of the scope of this paper, we decided to segment this surface manually. In this study, only the external surface of the deflated lung is considered.

A set of about 300 points were manually placed over the CBCT_{def} image along the surface of the deflated lung. The distance between points varied with the local curvature of the deflated surface, ranging roughly from 10 mm to 30 mm. MeshLab (Cignoni et al., 2008) was used to reconstruct a triangular surface from these points. First, the convex-hull of the point cloud provided an initial estimation of the surface. Then, a high resolution cloud of evenly spaced points was sampled from this initial surface using the Poisson disk sampling algorithm (Corsini et al., 2012). Finally, the ball-pivoting algorithm (Bernardini et al., 1999) was used to reconstruct a surface from the sampled point cloud. This latter algorithm forms triangles each time a ball of a predefined radius touches three points without containing any other point. This complete procedure allowed the reconstruction of a refined surface of triangles from a sparse cloud of manually placed points. It is worth noting that because of the convex-hull algorithm, all concave details from the initial point cloud (such as lobe sliding and fissure opening) were not reconstructed. However, this goes in accordance with our single structure assumption for representing the lung anatomy.

7.1.2. Estimation of the hilum deformation

During pneumothorax, the hilum deforms in the same direction that the lung deflates. The extent of this deformation is intervention-dependent and unknown *a priori*. In addition, regions of the lung parenchyma closest to the hilum are often totally collapsed by the pneumothorax. The image intensity of the hilum and the collapsed parenchyma become nearly indistinguishable. For these reasons, in this study, we used the deformation of the main airways as a surrogate for the hilum deformation. We estimated this airways deformation by means of intensity-based image registration. First, the three main level airways were semi-automatically segmented from the CBCT_{def} image. This segmentation was extended by 5 mm using morphological dilation in order to ensure the inclusion of airway contours (see purple contours on Fig. 4). Elastic registration between the rigidly registered CBCT_{inf} and the CBCT_{def} images was then performed using the NCC similarity metric

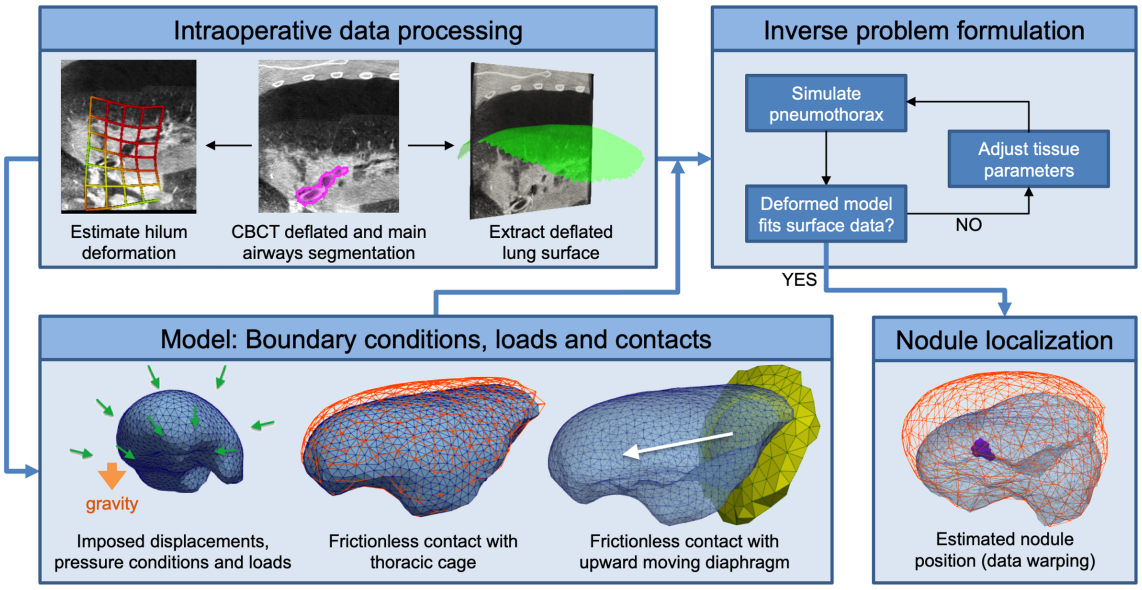

Figure 4: Schematic diagram of the *Phase 2* stage to estimate the pneumothorax deformation. Intraoperative images are processed to segment the surface of the deflated lung, and to compute a deformation field approximating the hilum deformation between CBCT_{inf} and CBCT_{def}. An inverse problem based on FE simulations estimated the pneumothorax deformation. Tissue parameters were optimized until the simulated model best fits the intraoperative data. Finally, the intraoperative nodule position is obtained by warping the undeformed position with the simulated pneumothorax deformation.

computed over the airways segmentation. The resulting deformation field was used as an estimation of the hilum deformation.

7.2. Simulation of the pneumothorax

Alveoli have a strong tendency to collapse caused by the inward recoil of their distended walls. These forces are present in varying degree at every moment during normal breathing. The reason why the lung does not collapse is because it gets pulled outwards by the chest wall and diaphragm, whose forces act on the lung surface thanks to the negative pressure in the pleural cavity. This outward pull corresponds to the transmural pressure, which is defined as the pressure gradient between the interior of the lung and the pleural cavity. At the end of expiration, these intrapleural and transmural pressures are estimated to -5 cm H_2O and to 5 cm H_2O, respectively (Levitzky, 2007).

During pneumothorax, the rupture of the chest wall resulting from surgical thoracic incisions creates a direct connection of the pleural cavity with the atmosphere. This increases the intrapleural pressure as air rushes in, until it becomes equal to the atmospheric pressure. This in turn decreases the transmural pressure that normally holds the lung open, which causes alveolar walls to collapse and squeeze air out of the lung. As illustrated in Fig. 5, the lung deflation during pneumothorax then occurs because the alveoli recoil forces become unopposed after the "disappearance" of outward-pulling forces at the surface of the lung. In addition, the deflating lung sags downwards under the effect of gravity.

A fully detailed modeling of the lung and pneumothorax phenomenon would require a stress-free model of the deflated lung loaded with all forces and pressures until equilibrium, which would be very complex. Therefore, we opted for a simpler functional approach in which the inflated lung at the end of expiration is considered stress-free, and the disappearance of the transmural pressure is approximated with a hydrostatic air pressure of the same amount

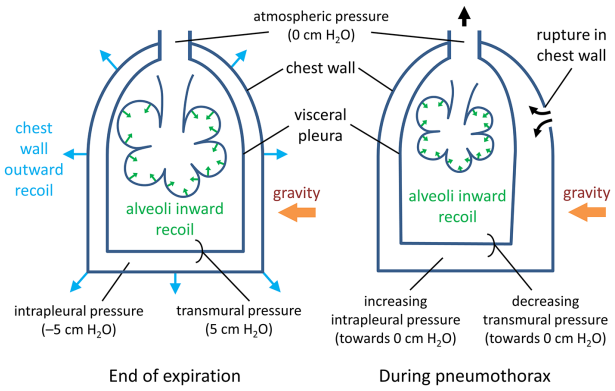

Figure 5: Schematic representation of the pneumothorax phenomenon. Left, at end of expiration the lung is in equilibrium and there is no airflow. Right, the rupture in the chest wall causes an increase of the intrapleural pressure and a decrease of the transmural pressure. The chest wall no longer pulls the surface of the lung outwards. The lung collapses due to alveoli inward recoil and gravity. The flow of air is indicated with black arrows.

(5 cm H_2O). This fixed pressure is applied as Dirichlet boundary conditions for the fluid domain at all surface nodes of the FE mesh. In combination with the fluid evacuation term $\kappa_b(p - p_c)$ of Eq. (9), this setup allows for pressure gradients to develop within the lung. Thanks to the effective-stress principle (Eq. (1)), these gradients induce shrinking internal forces similar to alveoli recoil. In other words, this approach produces lung deflation via compressive body forces at every material point, rather than normal forces applied at the lung surface.

7.2.1. Boundary conditions and loads

For the fluid domain, a fixed hydrostatic pressure of 5 cm H_2O was prescribed to all surface nodes through Dirichlet boundary conditions, whereas the remaining nodes were left with the natural no-flux boundary condition. As for the solid domain, nodes inside the main airways were constrained with imposed displacements coming from the estimation of the hilum deformation. Remaining nodes were left with the natural stress-free boundary condition. Finally, a gravitational load was applied to the whole porous medium in the lateral to medial direction (horizontal axis in the CBCT_{def} image).

7.2.2. Contact with the thoracic cage

Frictionless contact conditions were used to simulate the deforming lung sliding along the parietal pleura, *i.e.* the inner surface of the thoracic cage. This surface corresponds to the outer surface of the initial FE lung mesh, before simulation, that was re-sampled with a coarser mean triangle size of approximately 20 mm. This re-sampled surface, later referred as the contact surface, was assumed rigid throughout the simulations. Node-to-node frictionless contact conditions were prescribed on all surface nodes of the FE lung model, excluding the nodes with imposed displacement boundary conditions. These contact conditions restrict the deformation of the lung, and can be expressed using the following inequality constraints:

$$g(\boldsymbol{x}) \geq 0 \tag{12}$$

$$\sigma_n(\boldsymbol{x}) \leq 0 \tag{13}$$

$$g(\boldsymbol{x})\,\sigma_n(\boldsymbol{x}) = 0 \tag{14}$$

where $g(\boldsymbol{x})$ is the gap distance between the contact surface and the deformable surface at the material point $\boldsymbol{x}$; and $\sigma_n(\boldsymbol{x})$ is the applied normal contact force at the material point $\boldsymbol{x}$.

The gap distance is calculated as $g(\boldsymbol{x}) = g_0(\boldsymbol{x}) + \boldsymbol{u}(\boldsymbol{x}) \cdot \boldsymbol{v}$, where $\boldsymbol{v}$ is the inward pointing normal of the contact surface, $g_0(\boldsymbol{x})$ is the initial gap distance before deformation, and $\boldsymbol{u}(\boldsymbol{x})$ is the displacement vector. The distance $g(\boldsymbol{x})$ is thus negative when there is penetration of the deformable surface into the contact surface. The term $\sigma_n(\boldsymbol{x})$ is a shorthand notation for $(\boldsymbol{\sigma}(\boldsymbol{x})\,\boldsymbol{n}) \cdot \boldsymbol{n}$, the projection of the Cauchy traction at the material point $\boldsymbol{x}$ onto the outward pointing normal $\boldsymbol{n}$.

The Eqs. (12) to (14) correspond to the Signorini's conditions. The expression in Eq. (12) represents impenetrability, while Eq. (13) states that the contact forces must always be compressive. The complementary condition in Eq. (14) allows contact forces to be generated only during contact.

7.2.3. Contact with the upward moving diaphragm

During surgery, the use of curare (a muscle relaxant) relieves tension in the diaphragm that then

deforms under the pressure from abdominal organs. This deformation is transferred to the lung parenchyma which moves upwards towards the apex. Although this phenomenon is clinically observed for all patients, those with higher indices of obesity undergo larger diaphragm displacement.

During intraoperative imaging, the position of the diaphragm is not always in the FOV of the CBCT images. We thus introduced an additional contact surface representing the diaphragm that can push the lung model upwards during the FE simulations. This diaphragm contact surface was initialized as the lower surface of the initial FE lung mesh, before simulation, that was re-sampled with a coarser mean triangle size of approximately 20 mm. Since the position of this diaphragm surface was unknown in the intraoperative CBCT images, we defined its position with an additional parameter d_{diaph}. The surface is allowed to move towards the apex along the principal axis of the lung's geometry, which was computed using Principal Component Analysis (PCA) on the mesh nodes. d_{diaph} represent the distance, along the vertical axis, between the current diaphragm position and its initial position. This displacement was included in the parameters to be optimized by our inverse problem formulation, with a minimum value of 15 mm defined empirically by clinical observation.

7.2.4. Material properties

The lung tissue was considered as an isotropic and homogeneous poroelastic continuum. An important characteristic of our pneumothorax modeling approach is the allowance of air evacuation. We hypothesized that during pneumothorax air exchanges happen at the level of small bronchi, resulting in air being transported out of the porous medium through the airways. These exchange effects were approximated by an organ-wide distributed term $\kappa_b(p - p_c)$ that allowed the simulation of air evacuation (Eq. (9)). In addition, we hypothesized that tissue porosity may change from patient to patient according to his/her response to general anesthesia and mechanical ventilation, and the amount of atelectasis. The values for tissue porosity and intrabronchi permeability are unknown for every particular surgery, and were then included in the parameters to be optimized by our inverse problem formulation. For the remaining material properties, values and ranges reported in previous studies were chosen (Alvarez et al., 2019a; Kay Sun et al., 2014; Seyfi Noferest et al., 2018). Table 1 collects the values used during the pneumothorax simulations.

Table 1: Material properties and their values during pneumothorax simulations. The last three parameters are patient and intervention specific and varied within the reported range during an optimization process.

Parameter	Value	Units
E	550	Pa
ν	0.35	-
α	1.0	-
ρ_s	700	kg / m^3
ρ_f	1.205	kg / m^3
κ	2.75×10^{-17}	m^2
μ_f	1.83×10^{-5}	Pa·s
p_c	0	Pa
$\boldsymbol{g}$	9.81	m / s^2
ϕ	[0.00 , 0.93]	-
κ_b	$[1.0 \times 10^{-14}$, $1.0 \times 10^{-4}]$	1 / Pa·s
d_{diaph}	$[15 \times 10^{-3}$, $40 \times 10^{-3}]$	m

7.3. Inverse problem formulation

The amount of pneumothorax deformation observed during a VATS intervention is patient and intervention dependent. This difference in deformation can be translated as different values for specific model parameters. Since these values are unknown in advance, we proposed to estimate them using an inverse problem formulation. The goal was to simulate several pneumothorax deformations and to optimize the parameters until the model best reproduces the observed intraoperative deformation.

The trust-region non-linear optimization method was used to solve the inverse problem. The cost function was defined as a surface-to-surface distance between the lung deflated surface, segmented from the CBCT$_{def}$ image (*c.f.* Sec. 7.1.1), and the simulated lung deformed surface. Formally, we solved the fol-

lowing problem:

$$\arg\min_{\boldsymbol{\theta}} \ \Omega(\boldsymbol{\theta}) = \frac{1}{N}\sum_{i=1}^{N} \|\boldsymbol{p}_i - \boldsymbol{q}_i(\boldsymbol{\theta})\|^2 \qquad (15)$$

where $\boldsymbol{\theta}$ is a set of tissue parameters and Ω the surface-to-surface distance. N is the total number of nodes in the target surface segmented in CBCT_{def}, $\boldsymbol{p}_i$ is an indexed node of that surface and $\boldsymbol{q}_i(\boldsymbol{\theta})$ is its corresponding closest node on the surface of the deformed FE mesh.

Since the optimization may be highly sensitive to initialization, we repeated the process three times with a different initialization parameter vector $\boldsymbol{\theta}_0$. Values were each time randomly generated from realizations of uniform distributions with empirically-defined ranges (see Table 1). In this study all three simulations were always consistent, and only the first simulation results were reported in the results section.

7.4. Nodule localization

Tissue parameters ($\boldsymbol{\theta}$) that solve the optimization problem defined in Eq. (15) produce the lung deformation that more closely approaches the intraoperative observed lung surface. The associated deformation field is defined on a spatial domain bounded by the FE mesh, and can be computed at any point by means of barycentric interpolation. This interpolation was used to warp the preoperative CT, which provided an estimation of the nodule position after pneumothorax.

8. Results

This section presents and comments on the quantitative and qualitative findings from this study. The clinical dataset used for validation is first described, followed by the evaluation of the deformation estimated after the change of pose (*Phase 1*) and pneumothorax (*Phase 2*).

8.1. Clinical dataset

Our retrospective study included five patients with single pulmonary nodules detected by CT examination. All were enrolled for a VATS wedge resection guided by intraoperative CBCT imaging. Our experimental protocol is an extension of the original work introduced by Rouzé et al. (2016), with two CBCT acquisitions instead of one, one before and one after induction of the pneumothorax. This study was performed at Rennes University Hospital (France) with the approval of the local ethics committee (2016-A01353-48 35RC16_9838). All patients signed an informed consent before surgery.

The preoperative CT is the standard diagnostic image. This image was acquired under breath-hold at end-of-inhalation and with the patient in supine position. During surgery, all patients were anesthetized and intubated with a double lumen tube (Bronchocath, Mansfield, MA, USA) that allows independent ventilation of the operated and non-operated lungs. Both CBCT images were acquired with a C-arm system (Artis Zeego, Siemens Healthcare, Germany) after general anesthesia and mechanical ventilation, with the patient in *lateral decubitus* position. The first CBCT image (CBCT_{inf}) was acquired before the creation of surgical incisions, with the operated lung still inflated; ventilation was momentarily stopped at the end of expiration. The second CBCT image (CBCT_{def}) was acquired after pneumothorax, with the operated lung deflated. The amount of lung deflation was controlled to provide sufficient space for maneuvering during surgery while avoiding total lung collapse. This was achieved by means of two mechanisms. For the first mechanism, patients were put under single-lung ventilation (breathing through the non-operated lung only) and air entered naturally into the pleural cavity through the thoracic incisions. The amount of deflation was controlled by insufflating oxygen into the operated lung through the lumen of the tube. For the second mechanism, airtight trocars were used and CO_2 was insufflated into the pleural cavity with the patient under double-lung ventilation. The amount of deflation was controlled by modulating the CO_2 pressure.

For validation purposes, paired anatomical landmarks were manually placed on the CT, CBCT_{inf} and CBCT_{def} images. This was performed by a single rater, the expert thoracic surgeon who performed all the VATS interventions. A total of 23 to 45 landmarks were placed for each patient. These landmarks

Table 2: Study characteristics for each clinical case. The pneumothorax was controlled following two techniques: mechanical control of air inflow into the lung through the intubation tube; or pressurized insufflation of CO_2 into the thoracic cage through airtight trocars. The number of validation landmarks depends on the visibility of lung structures in the images.

Case	Operated lung	Pneumothorax	# landmarks
1	Left	Air	27
2	Right	Air	40
3	Right	Air	46
4	Right	Air	23
5	Left	CO_2	23

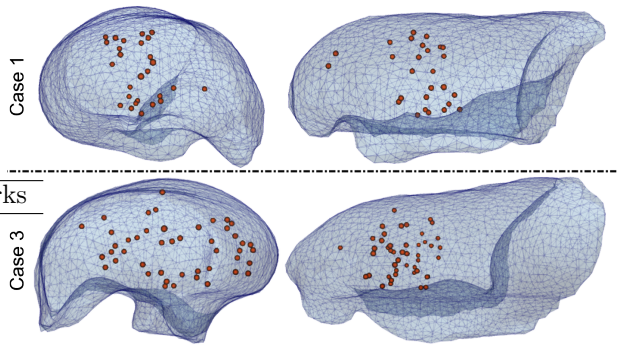

Figure 6: Spatial distribution of anatomical landmarks within the lung FE mesh reconstructed from the preoperative CT image.

were distributed among vessel and airway bifurcations in the most complex image, *i.e.* the $CBCT_{def}$ image, and then were localized in the $CBCT_{inf}$ and CT images. The validation was based on Target Registration Errors (TRE) computed as the distance between corresponding landmarks after deformation compensation. Differences among TRE distributions were tested with the non parametric Wilcoxon signed rank test, with a confidence level of 5%. The study characteristics for each clinical case are detailed in Table 2.

Landmark positions are illustrated in two representative cases in Fig. 6. Since these anatomical landmarks are used for validation, their positions should be distributed inside the lung parenchyma as homogeneously as possible. However, the restrictions of the image quality were difficult to surpass and reduced the spatial distribution of these landmarks in some cases. Notably, structures of medium-size and below that are clearly visible in the preoperative CT image were impossible to locate in the $CBCT_{def}$ image. It is clear from Fig. 6 that validation can only be performed for regions of the lung inside the FOV of the CBCT scans. Notably, regions of the apex and diaphragm do not contain any landmarks.

8.2. Results: Phase 1, estimation of the change of pose

The change of pose deformation estimation relies heavily on the computation of a deformation field through intensity based image registration. The accuracy of this deformation field was evaluated with TRE distributions computed from the landmarks of the preoperative CT and intraoperative $CBCT_{inf}$ images. Figure 7 depicts the obtained TRE distributions for all clinical cases. First, rigid registration provided an insight on the amount of deformation induced by the change of patient pose. We could observe large deformations, with the main structures in major miss-alignment. We obtained mean ($\pm$ standard deviation) TREs of 6.8 mm ($\pm$1.9 mm), 12.1 mm ($\pm$4.1 mm), 13.5 mm ($\pm$3.2 mm), 25.8 mm ($\pm$5.0 mm), and 18.0 mm ($\pm$7.1 mm) for cases 1 to 5, respectively. These errors are even larger than those reported for respiratory motion in the lung registration literature (*e.g.* a mean error of 8.4 mm reported by Delmon et al. (2013)). After elastic registration, TREs were significantly reduced to mean values of 1.5 mm ($\pm$1.4 mm), 1.0 mm ($\pm$0.5 mm), 1.6 mm ($\pm$1.4 mm), 2.7 mm ($\pm$2.7 mm), 1.6 mm ($\pm$1.4 mm), respectively. This registration accuracy is comparable to the one reported in studies for lung breathing motion compensation (Murphy et al., 2011).

Fig. 8 depicts the results obtained after rigid and elastic registration. Coronal slices of the registered CT and intraoperative $CBCT_{inf}$ images were superposed to show the quality of registration on two representative clinical cases. It can be observed that internal structures were within reasonable alignment, as suggested by the obtained TRE distributions. Also, lung contours were well aligned thanks to the masking approach used during registration. However, we

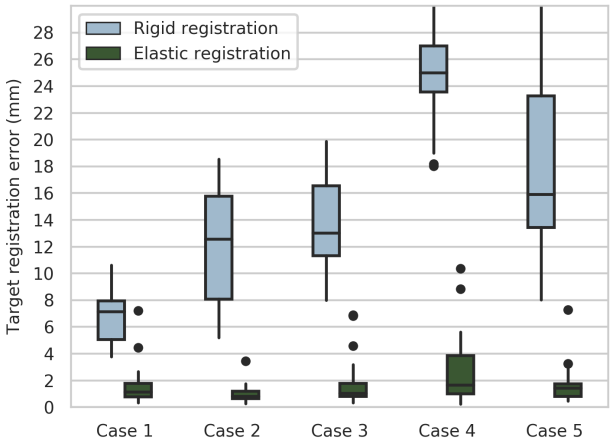

Figure 7: TRE distributions for rigid and elastic registration between the preoperative CT and intraoperative CBCT$_{inf}$ (*Phase 1*, change of pose).

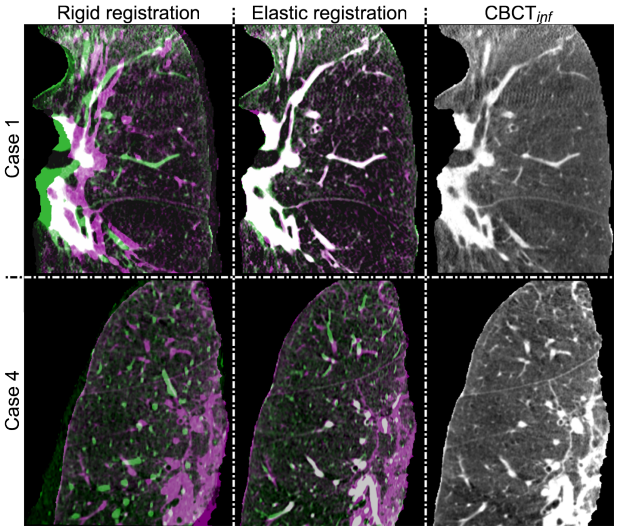

Figure 8: Qualitative results of rigid and elastic registration between the preoperative CT (green) and intraoperative CBCT$_{inf}$ (magenta) images. Coronal slices are shown for two representative cases. The target CBCT$_{inf}$ image in gray-scale is shown in the far right column.

found poorly-registered regions near the rim of the CBCT$_{inf}$ images, where the lung is incomplete because of the limited FOV of the scanner and where reconstruction artefacts were present (*e.g.* Case 1). Furthermore, localized atelectasis also reduced the registration quality, since voxel intensities drastically differed between images in the affected regions (*e.g.* Case 4). These registration errors may be underrepresented in the TRE distributions of Fig. 7 given the difficult landmark placement in these regions. However, we consider that the achieved registration accuracy is sufficient for the purpose of estimating the complete lung geometry after the change of pose.

Due to the lack of landmarks outside the FOV of the CBCT images, it was not possible to directly evaluate the quality of the complete lung geometry after FEM extrapolation. Nonetheless, the benefit of this extrapolation approach was assessed in comparison to a baseline rigid registration approach, and the results are presented later in Sec. 8.4.

8.3. Results: Phase 2, estimation of the pneumothorax

The solution to the inverse problem formulation was used to warp the CBCT$_{inf}$ landmarks with barycentric interpolation. The TRE distributions were computed using these deformed landmarks and the ground truth CBCT$_{def}$ landmarks. To illustrate our contribution, the errors that would be obtained without a deformation compensation method were also estimated in two ways. First, TREs between the rigidly registered CT and CBCT$_{def}$ images were computed. This corresponds to the errors expected when the CBCT$_{inf}$ image is not available and only a rigid transformation of the preoperative data to the intraoperative setting is possible. Second, TREs were computed between the rigidly registered CBCT$_{inf}$ and CBCT$_{def}$ images. These would be the expected errors when estimating the nodule position directly from the CBCT$_{inf}$ image, without compensating for the pneumothorax deformation. These TRE distributions are presented for all clinical cases in Fig. 9.

Figure 9 first puts in evidence the large lung deformation that occurs during a VATS procedure. After rigid registration of the preoperative CT and intraoperative CBCT$_{def}$ images, we obtained mean TREs of 33.8 mm (±10.1 mm), 34.1 mm (±3.7 mm), 22.0 mm (±8.9 mm), 34.4 mm (±4.6 mm), and 37.9 mm

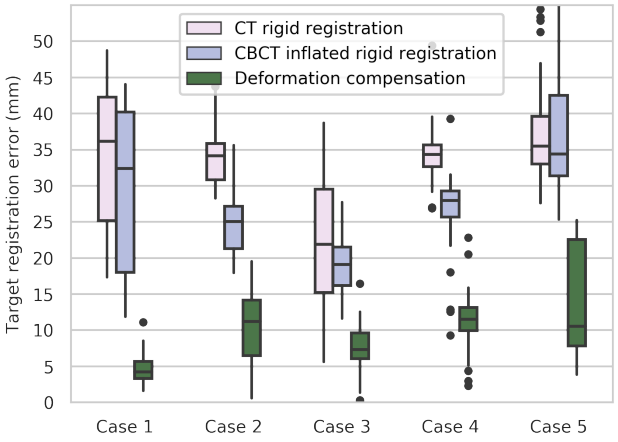

Figure 9: TRE distributions for our complete deformation compensation framework, alongside the errors expected without deformation compensation. These latter distributions correspond to rigidly registering the preoperative CT with the CBCT_{inf} and CBCT_{def} images, respectively.

(±8.2 mm) for cases 1 to 5, respectively. Likewise, mean TREs after rigid registration of the CBCT_{inf} and CBCT_{def} images were 28.7 mm (±11.6 mm), 24.6 mm (±4.0 mm), 19.5 mm (±4.0 mm), 25.9 mm (±6.8 mm), and 37.7 mm (±8.8 mm). This deformation is considerably larger than both breathing and change of pose deformations. Except for Case 5, larger deformations were obtained from rigidly registering the preoperative CT image instead of the CBCT_{inf} image (maximum $p = .018$). This result corroborates that the change of patient pose does have an influence in lung deformation during VATS. Also, it is clear from Fig. 9 that our deformation compensation framework is able to account for a considerable amount of this intraoperative deformation. Indeed, mean TREs were reduced to 4.9 mm (±2.2 mm), 10.3 mm (±5.2 mm), 7.5 mm (±3.3 mm), 11.2 mm (±4.9 mm), and 14.3 mm (±7.5 mm), respectively, which corresponds to a correction of 85%, 70%, 68%, 68%, and 63% (71% in mean) of the initial error without compensation. Specifically, the nodule localization errors were 8.4 mm, 13.4 mm, 9.9 mm, 11.6 mm and 10.2 mm, respectively.

Figure 10 illustrates quantitative results for two clinical cases. It can be observed that the surfaces of the deformed FE meshes were close to the intraoperative deflated surfaces without fitting them perfectly. This is a consequence of the chosen simplified approach to model the complex lung deformation. For instance, the constant fluid pressure boundary conditions generated highly symmetrical and homogeneous lung deformation, given that the contribution of the fluid medium to total stress is purely volumetric. This symmetry was only constrained by the shape of the estimated lung geometry (*i.e.* the deformable FE mesh and contact surfaces) and the direction of gravity, which may be oversimplifying. For Case 2, lobes also deform very independently from each other, which is currently not taken into account for modeling pneumothorax deformation. Finally, it can also be observed in Fig. 10 that the landmarks with the lowest registration errors were those closest to the hilum. These better results in the hilum area can be explained by the hilum deformation estimation step, which was based on intensity-based registration of the main airways.

The tissue parameters obtained from our inverse problem formulation are listed in Table 3. The optimization process resulted in values for the intrabronchi permeability (κ_b) and tissue porosity (ϕ) that were consistent with a previous study (Alvarez et al., 2019a). As for the diaphragm upward displacement (d_{diaph}), we could observe that besides Case 1, a value of 15 mm was found for all clinical cases. This value corresponds to the lower bound of the range specified during optimization, meaning that a higher diaphragm displacement only increased the distance from the FE deformed mesh and the target intraoperative deflated lung surface in these clinical cases.

The complete deformation compensation framework allows the warping of the preoperative CT image with the FE deformed meshes issued from *Phase 1* and *Phase 2*. This warped CT image is shown in Fig. 11 along with the preoperative CT, CBCT_{inf} and CBCT_{def} images, for two representative cases. Color contours are used to illustrate the changing shape of the FE lung mesh through the deformation compensation stages: before change of pose (cyan), after change of pose (orange), and after change of pose and pneumothorax (purple). It can be observed

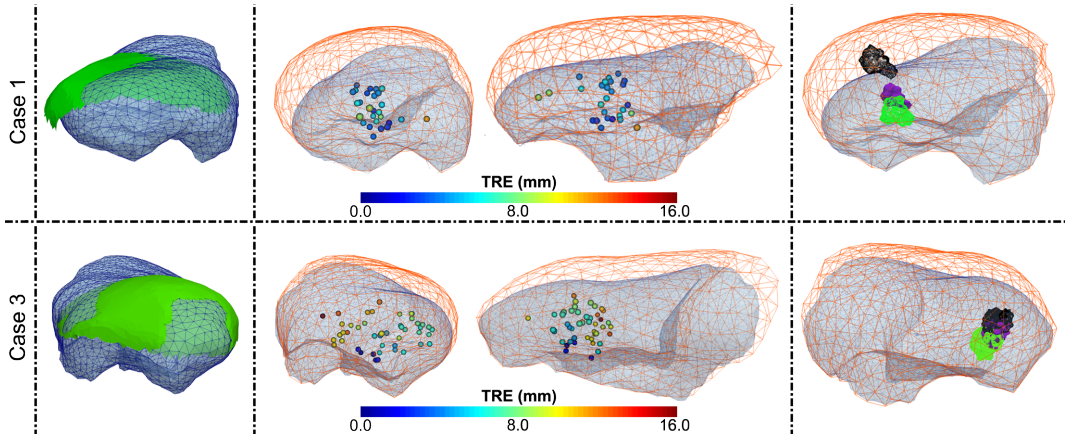

Figure 10: Qualitative results of our deformation compensation framework for two clinical cases. Left: final deformed lung FE mesh superposed over the extracted deflated lung surface (in green). Middle: Registered landmark errors, deformed FE lung mesh and thoracic cage contact surface. Right: Initial nodule position (wireframe, black surface), ground truth nodule position (wireframe, green surface) and predicted nodule position (solid, purple surface). Results for all cases are available in the online supplementary materials.

Table 3: Tissue parameters estimated from our inverse problem optimization approach: intrabronchi permeability (κ_b), tissue porosity (ϕ), and diaphragm upward displacement (d_{diaph}).

Case	κ_b (1 / Pa s)	ϕ (unitless)	d_{diaph} (m)
1	14.44×10^{-9}	0.56	20.41×10^{-3}
2	95.31×10^{-9}	0.79	15.00×10^{-3}
3	2.61×10^{-9}	0.82	15.00×10^{-3}
4	1.23×10^{-9}	0.37	15.00×10^{-3}
5	37.29×10^{-9}	0.64	15.00×10^{-3}

that the diaphragm is completely out of the FOV of both CBCT images for Case 1, and is only barely visible in the CBCT$_{def}$ image for Case 2. Also, the cranio-caudal misalignment between both CBCTs can be very important, as seen for Case 2, reducing significantly the overlap between the intraoperative images. In terms of deformation compensation, it can be observed for Case 1 that the estimated deflated lung surface is well aligned with the CBCT$_{def}$ deflated surface. Also, the cranio-caudal height of the oblique fissure fits well with its actual position. These results are consistent with the mean TRE measured below 5 mm. For Case 2, however, the estimated deformation is clearly poorer. In this highly complex case, the lung lobes deformed independently during pneumothorax, resulting in the opening of both fissures and a highly heterogeneous lung deflation. Furthermore, the lower lobe deflated more than the other two lobes, causing a significant amount of atelectasis. While the mean TRE is reduced from 34 mm to 10 mm, the estimated deformed lung is too regular in comparison with its actual shape. While our compensation framework seems promising for several cases, further investigations will be necessary for such complex deformations.

8.4. Variants of the method

The relevance of the main components of our deformation compensation framework was investigated using variant implementations presented in this section.

8.4.1. Influence of the change of pose and hilum estimation

Three variants of our method were implemented to assess the influence of the change of pose and hilum deformation estimation processing steps:

(A) *No change of pose*: neither the change of pose deformation nor the hilum deformation between

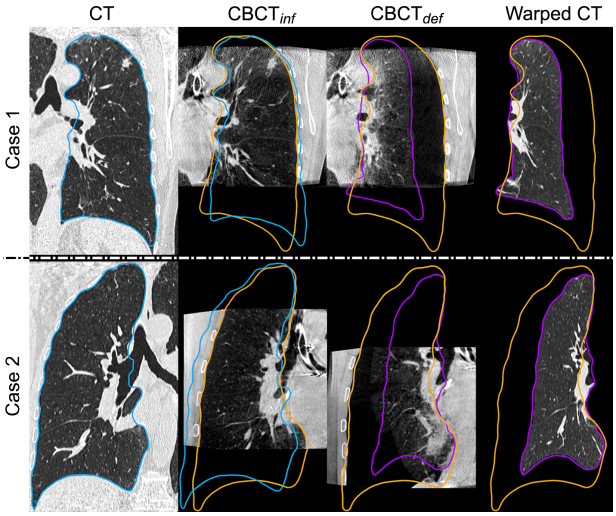

Figure 11: Qualitative results of our deformation compensation framework for two representative cases. The CT and CBCT$_{inf}$ images are rigidly registered to the CBCT$_{def}$ image. Coronal slices of exactly the same region of interest are shown for all images. The color contours illustrate the position of the FE mesh at the beginning of *Phase 1* (cyan) and *Phase 2* (orange), as well as at the end of *Phase 2* (purple). Results for all cases are available in the online supplementary materials.

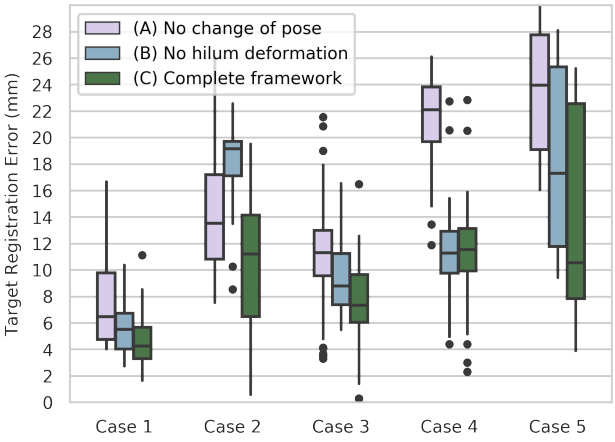

Figure 12: TRE distributions for three variants of the proposed lung deformation compensation method.

the CBCT$_{inf}$ and CBCT$_{def}$ images were taken into account. The preoperative CT image was simply rigidly registered to the CBCT$_{def}$ image using the spine as the reference, as in Sec. 6.1.1. The transformed lung segmentation was used to generate the lung FE mesh and to define contact surfaces. Boundary conditions were prescribed as in Sec. 7.2, with the exception of the imposed displacements in the airway inlet that were replaced with fixed boundary conditions ($\boldsymbol{u} = \mathbf{0}$).

(B) *No hilum deformation*: the change of pose deformation was taken into account but the hilum deformation between both CBCT images was not compensated. Since no deformation field mapping the airways before and after pneumothorax was available, fixed boundary conditions were applied at the airway inlet ($\boldsymbol{u} = \mathbf{0}$). The remaining boundary conditions, intraoperative geometry and contact conditions were applied as described in Sec. 7.2.

(C) *Complete framework*: This variant corresponds to the implementation of all the methods described in Sec. 7.2.

The TRE distributions of each variant are presented in Fig. 12. With the exception of Case 2, a significant improvement can be observed of variant (B) over (A) across cases (maximum $p = .006$). Likewise, variant (C) provided better results than variant (B) (maximum $p = .019$), except for Case 4. These results suggest that all processing steps of the complete deformation compensation framework are important. Even though the amount of change of pose and hilum deformation varies among cases, taking these deformations into account allows for a better final estimation.

8.4.2. Influence of the moving diaphragm

Another important element of our deformation compensation framework is the modeling of the diaphragm movement. Its influence was evaluated by comparing the results of the complete framework with and without nullifying the diaphragm movement, *i.e.* fixing $d_{diaph} = 0$ mm. The results are shown in Fig. 13. Modeling the diaphragm upward movement significantly reduced TREs for Cases 1, 3,

and 4 (maximum $p < .001$). However, the estimation accuracy remained unchanged for Case 5 and actually decreased for Case 2 ($p = .002$). For this complex case, the estimated diaphragm position after the change of pose compensation roughly matched the actual diaphragm position barely visible in the CBCT$_{def}$ image (see Fig. 11). Therefore, any positive displacement of the diaphragm (d_{diaph}) would worsen estimation accuracy.

It should be noted that for all clinical cases except Case 1, the displacement d_{diaph} of the optimal solution was 15 mm, namely the minimum value allowed during the optimization process. However, an observation of the predicted landmark positions with respect to the ground truth landmarks suggests that deformation compensation errors may be partially explained by a miss-prediction of this diaphragm movement. An explanation could reside in the antagonism between a diaphragm upward movement and the cost function of the optimization problem: moving the diaphragm upwards tends to enlarge the lung outwards, in the opposite direction of lung deflation, therefore increasing the surface-to-surface cost function distance.

While the effects of our diaphragm model are still limited in several cases, our results suggest that accounting for the diaphragm movement, even empirically, could allow for a better estimation of the intraoperative deflated lung shape.

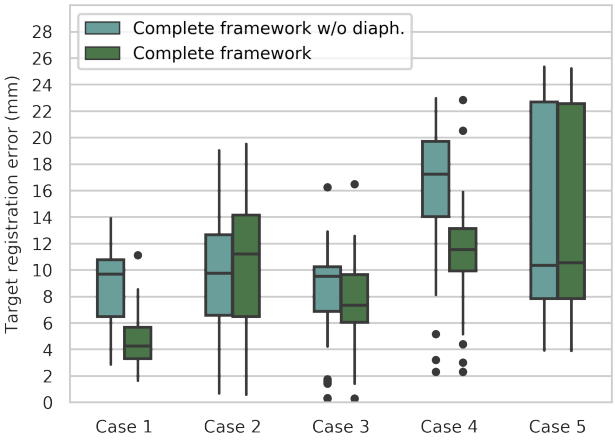

Figure 13: TRE distributions for our deformation compensation framework with and without including the upward diaphragm movement.

9. Discussion

Advantages, limits, and perspectives of the main components of the proposed method are discussed in this section.

9.1. Hybrid approach to deformation estimation

In this study, we used intensity-based image registration to estimate displacement boundary conditions for FEM lung simulations of change of pose and pneumothorax deformation. This hybrid approach was crucial for the estimation of complex lung deformation that would have been more difficult, if not impossible, using purely intensity-based or FEM strategies. For *Phase 1*, we estimated the change of pose deformation between the preoperative CT and the intraoperative CBCT$_{inf}$ images with an algorithm that accounts for sliding at the lung interface (Wu et al., 2008). We found the magnitude of this deformation to be consistent with values reported in a previous study (Alvarez et al., 2018). For *Phase 2*, the hilum deformation was approximated by registering the main airways of the intraoperative CBCT$_{inf}$ and CBCT$_{def}$ images. Final results suggest that even though approximative, this approach provides better estimations than alternatives not taking into account hilum deformation. To go further, it will be necessary to better capture the non-homogeneous variations of the hilum deformation. This is quite challenging due to the occurrence, to date unpredictable, of very localized atelectasis after pneumothorax. This collapsing of the airways results in severe intensity and textural discrepancies of the CBCT images before and after pneumothorax, which are difficult to cope with using traditional segmentation and registration methods. We believe, however, that these challenges may be overcome thanks to the efforts recently put forward by the community, with registration algorithms not requiring prior segmentation (Heinrich et al., 2016) and/or relying on salient keypoints rather than image intensity (Ruhaak et al., 2017). Incorporating such approaches into our framework could lead

to substantial improvements that will be studied in future work.

9.2. Modeling choices

For the pneumothorax simulations, we used a poroelastic model of the lung with allowance for air evacuation. This approach follows the principle of effective stress that decomposes the total stress into fluid and solid stresses. This principle permits the macro-scale simulation of airflow-parenchyma interaction in a cost-effective manner. We hypothesized that the solid medium behaves as a homogeneous, linearly-elastic material undergoing small deformations. This assumption was supported by noting that pneumothorax deformation during our simulations was mainly caused by the stress generated from the fluid phase. Also, this simplified model is in principle computationally efficient, which would be important in the future to comply with the time restrictions of clinical practice. However, despite promising preliminary results, the lung deformation can be underestimated, for which several improvements can be investigated. For instance, we envision other constitutive laws for the solid medium, such as the Saint Venant-Kirchhoff model that does not linearize the strain tensor to allow for large displacements (Seyfi Noferest et al., 2018), or more complex hyperelastic nonlinear stress-strain relations (Berger et al., 2016). We will also assess the use of heterogeneous material properties estimated from measured lung deformation (Hasse et al., 2018).

In parallel to more adequate constitutive laws and tissue parameters, a major improvement would be expected with a multiple-lobes lung model as opposed to a single-structure lung model. As observed for Case 2, lobes can slide against each other, the fissures can open widely, or a combination of the two. Modeling such effects will be challenging, as not only they are technically difficult but also very unpredictable.

9.3. Inverse formulation approach

The inverse problem formulation based on the poroelastic lung model allowed the compensation of patient-specific and intervention-specific pneumothorax deformation. This was achieved by fitting the deformable lung model to the observed intraoperative surface of the deflated lung, changing tissue porosity (ϕ) and intrabronchi permeability (κ_b) parameters, as well as simulating the upward movement of the diaphragm (d_{diaph}). It should be acknowledged that our inverse problem formulation did not take into account internal lung structural information, which had a clear impact on the correct estimation of the upward moving diaphragm, and possibly the complete lung parenchyma. With improved processing of the CBCT images, it should be possible to include internal lung structures such as vessels (Cazoulat et al., 2016), salient keypoints (Ruhaak et al., 2017), or even the lobe boundaries, in the inverse problem formulation.

Finally, the inverse problem formulation currently minimizes the surface-to-surface distance between the deformable lung model and the intraoperative data in a least-squares sense. Since the proposed model has few degrees of freedom, the deformed lung surface does not exactly fit the intraoperative data. An alternative to this approach would be to use Lagrange multipliers to constrain the deformation so that surface nodes of the FE mesh fit local surface data (Morin et al., 2017).

9.4. Diaphragm movement

Clinically, it is known that the diaphragm tends to move upwards due to the surgical setup. This phenomenon was consistently observed on all cases, based on inner-lung landmark measurements. Therefore, a functional approach to model the diaphragm movement was introduced, with the d_{diaph} parameter as part of the optimization process. However, as shown in Sec. 8.4.2, a meaningful estimation of diaphragm movement could be obtained for one case only. Although several factors may be affecting this issue, we believe the definition of the cost function (Eq. (15)) to be among the most important. Indeed, currently, it relies on surface data only, which may not be well suited to compensate for longitudinal deformation. Improvements could consist in extracting the diaphragm surface when it is partially visible in the CBCT images (*e.g.* cases 4 and 2), and to include sub-surface information in the computation of the cost function, as mentioned above.

9.5. Towards clinical practice: practicability and accuracy

Since the aim of this study was to evaluate the capacity to compensate for lung deformation during VATS, we did not primarily focused on the clinical practicality. Therefore, several processes required manual interactions: the initialization of registration or segmentation algorithms, the refinement of segmentation masks, and the extraction of the CBCT_{def} deflated lung surface. In total, these interactions may take a considerable amount of time (more than 60 minutes for some cases), but we are confident that most of them can be replaced by dedicated image processing methods. Another important factor will be the computational efficiency. Although our intensity-based image registration steps are relatively efficient (10 to 15 minutes per case), our inverse problem formulation is computationally intensive (4 to 6 hours per case). This situation is expected to worsen when considering the methodological improvements discussed previously, since these may introduce further computations. Therefore, it will be necessary to find a trade-off between accuracy and efficiency, for which deformation atlas (Kay Sun et al., 2014) or learning-based FEM (Mendizabal et al., 2020) approaches will be investigated.

Finally, no standard criteria stand to date regarding the required accuracy for an intraoperative nodule localization algorithm. It is thus not straightforward to evaluate the significance of our current results. Nodules indicated for surgical resection are at least 8 mm in length, and small wedge resections are approximatively 3×4 cm. Considering these minimum sizes and our current nodule localization errors of 8 to 13 mm, these nodules should always be within the resection, at least partially, which is sufficient for diagnostic purpose. However, maximum errors could still be too large to guarantee the localization for every patient. A long-term objective, defined by our clinical partners, will be to achieve mean errors around 5 mm with maximum errors below 10 mm. This would also ensure sufficient negative margins of 15 mm as suggested by Wolf et al. (2017). Intraoperative process time should be kept under 15 minutes.

10. Conclusion

To our best knowledge, this is the first study to propose an intraoperative markerless lung nodule localization framework for VATS, which relies on a hybrid method combining intraoperative CBCT imaging, intensity-based image registration, and biomechanical modeling techniques. We proposed to decouple the very challenging problem of intraoperative deformation estimation into two more tractable subproblems: estimating the change of pose deformation (*Phase 1*) and then estimating the pneumothorax deformation (*Phase 2*). We were able to demonstrate the feasibility of our deformation compensation framework on 5 retrospective clinical cases of patients who underwent a VATS intervention. Average initial errors in the range of 22 to 38 mm were reduced to the range of 4 to 14 mm, which corresponds to a correction of 63 to 85% of the error without compensation (71% in mean).

To improve the methods towards errors consistently under the 5 mm objective, future works will be mostly focused on allowing for lobes separation within the model and taking into account sub-surface lung information to drive the simulations. Another challenge will be to acquire a single CBCT scan instead of two (only CBCT_{def} after lung deflation) to simplify the procedure and limit the radiation dose. Finally, our overall objective aims at overlaying the simulated deformed lung and the nodule position over the CBCT image, and ultimately in real time in the endoscopic view. By removing the need for a preoperative nodule marking localization procedures and its associated risks, and increasing the resection accuracy, the proposed method could significantly benefit the clinical practice in thoracoscopic surgery.

Acknowledgements

This work was supported by the *Région Bretagne* through its *Allocations de Recherche Doctorale* (ARED) framework; the French National Research Agency (ANR) through the frameworks *Investissements d'Avenir Labex CAMI* (ANR-11-LABX-0004), *Infrastructure d'Avenir en Biologie et Santé* (ANR-11-INBS-0006) and *VATSop* (ANR-20-CE19-0015);

and the National Institutes of Health - NINDS grant R01NS049251.

References

Al-Mayah, A., Moseley, J., Brock, K.K., 2008. Contact surface and material nonlinearity modeling of human lungs. Phys Med Biol 53, 305–317.

Al-Mayah, A., Moseley, J., Velec, M., Brock, K., 2011. Toward efficient biomechanical-based deformable image registration of lungs for image-guided radiotherapy. Phys Med Biol 56, 4701–4713.

Al-Mayah, A., Moseley, J., Velec, M., Brock, K.K., 2009. Sliding characteristic and material compressibility of human lung: Parametric study and verification. Med Phys 36, 4625–4633.

Al-Mayah, A., Moseley, J., Velec, M., Hunter, S., Brock, K., 2010. Deformable image registration of heterogeneous human lung incorporating the bronchial tree. Med Phys 37, 4560–4571.

Alvarez, P., Chabanas, M., Rouzé, S., Castro, M., Dillenseger, J.L., Payan, Y., 2018. Lung deformation between preoperative CT and intraoperative CBCT for thoracoscopic surgery: a case study, in: Medical Imaging 2018: Image-Guided Procedures, Robotic Interventions, and Modeling, Houston, United States. p. 40.

Alvarez, P., Narasimhan, S., Rouzé, S., Dillenseger, J.L., Payan, Y., Miga, M.I., Chabanas, M., 2019a. Biphasic model of lung deformations for video-assisted thoracoscopic surgery (VATS), in: 2019 IEEE 16th International Symposium on Biomedical Imaging (ISBI 2019), IEEE, Venice, Italy. pp. 1367–1371.

Alvarez, P., Rouzé, S., Chabanas, M., Payan, Y., Dillenseger, J.L., 2019b. Image-based registration for lung nodule localization during VATS, in: Surgetica 2019, Rennes, France.

Berger, L., Bordas, R., Burrowes, K., Grau, V., Tavener, S., Kay, D., 2016. A poroelastic model coupled to a fluid network with applications in lung modelling. Int J Numer Meth Bio 32, n/a–n/a.

Bernardini, F., Mittleman, J., Rushmeier, H., Silva, C., Taubin, G., 1999. The ball-pivoting algorithm for surface reconstruction. IEEE Trans Vis Comput Graph 5, 349–359.

Biot, M.A., 1941. General theory of three-dimensional consolidation. J Appl Phys 12, 155–164.

Biot, M.A., 1955. Theory of elasticity and consolidation for a porous anisotropic solid. J Appl Phys 26, 182–185.

Bray, F., Ferlay, J., Soerjomataram, I., Siegel, R.L., Torre, L.A., Jemal, A., 2018. Global cancer statistics 2018: GLOBOCAN estimates of incidence and mortality worldwide for 36 cancers in 185 countries. CA Cancer J Clin 68, 394–424.

Cazoulat, G., Owen, D., Matuszak, M.M., Balter, J.M., Brock, K.K., 2016. Biomechanical deformable image registration of longitudinal lung CT images using vessel information. Phys Med Biol 61, 4826–4839.

Chao, Y.K., Leow, O.Q.Y., Wen, C.T., Fang, H.Y., 2019. Image-guided thoracoscopic lung resection using a dual-marker localization technique in a hybrid operating room. Surg Endosc 33, 3858–3863.

Chao, Y.K., Pan, K.T., Wen, C.T., Fang, H.Y., Hsieh, M.J., 2018. A comparison of efficacy and safety of preoperative versus intraoperative computed tomography-guided thoracoscopic lung resection. J Thorac Cardiov Sur 156, 1974–1983.e1.

Chen, I., Coffey, A.M., Siyi Ding, Dumpuri, P., Dawant, B.M., Thompson, R.C., Miga, M.I., 2011. Intraoperative Brain Shift Compensation: Accounting for Dural Septa. IEEE Transactions on Biomedical Engineering 58, 499–508.

Cignoni, P., Callieri, M., Corsini, M., Dellepiane, M., Ganovelli, F., Ranzuglia, G., 2008. Meshlab: an open-source mesh processing tool, in: Scarano, V., Chiara, R.D., Erra, U. (Eds.), Eurographics Italian Chapter Conference, The Eurographics Association.

Corsini, M., Cignoni, P., Scopigno, R., 2012. Efficient and flexible sampling with blue noise properties of triangular meshes. IEEE Trans Vis Comput Graphics 18, 914–924.

Crum, W.R., Camara, O., Hawkes, D.J., 2007. Methods for inverting dense displacement fields: Evaluation in brain image registration, in: Medical Image Computing and Computer-Assisted Intervention – MICCAI 2007, pp. 900–907.

Delmon, V., Rit, S., Pinho, R., Sarrut, D., 2013. Registration of sliding objects using direction dependent B-splines decomposition. Phys Med Biol 58, 1303–1314.

Dumpuri, P., Thompson, R.C., Dawant, B.M., Cao, A., Miga, M.I., 2007. An atlas-based method to compensate for brain shift: Preliminary results. Med. Image Anal. 11, 128–145.

Eom, J., Xu, X.G., De, S., Shi, C., 2010. Predictive modeling of lung motion over the entire respiratory cycle using measured pressure-volume data, 4DCT images, and finite-element analysis. Med Phys 37, 4389–4400.

Falcoz, P.E., Puyraveau, M., Thomas, P.A., Decaluwe, H., Hürtgen, M., Petersen, R.H., Hansen, H., Brunelli, A., 2016. Video-assisted thoracoscopic surgery versus open lobectomy for primary non-small-cell lung cancer: a propensity-matched analysis of outcome from the European Society of Thoracic Surgeon database. Eur J Cardio-Thorac 49, 602–609.

Fuerst, B., Mansi, T., Carnis, F., Salzle, M., Zhang, J., Declerck, J., Boettger, T., Bayouth, J., Navab, N., Kamen, A., 2015. Patient-specific biomechanical model for the prediction of lung motion from 4-D CT images. IEEE Trans Med Imag 34, 599–607.

Gill, R.R., Zheng, Y., Barlow, J.S., Jayender, J., Girard, E.E., Hartigan, P.M., Chirieac, L.R., Belle-King, C.J., Murray, K., Sears, C., Wee, J.O., Jaklitsch, M.T., Colson, Y.L., Bueno, R., 2015. Image-guided video assisted thoracoscopic surgery (iVATS) - phase i-II clinical trial. J Surg Oncol 112, 18–25.

Han, L., Dong, H., McClelland, J.R., Han, L., Hawkes, D.J., Barratt, D.C., 2017. A hybrid patient-specific biomechanical model based image registration method for the motion estimation of lungs. Med Image Anal 39, 87–100.

Hasse, K., O'Connell, D., Min, Y., Neylon, J., Low, D.A., Santhanam, A., 2018. Estimation and validation of patient-specific high-resolution lung elasticity derived from 4DCT. Med Phys 45, 666–677.

Heinrich, M.P., Simpson, I.J., Papież, B.W., Brady, S.M., Schnabel, J.A., 2016. Deformable image registration by combining uncertainty estimates from supervoxel belief propagation. Medical Image Analysis 27, 57–71.

Henschke, C.I., McCauley, D.I., Yankelevitz, D.F., Naidich, D.P., McGuinness, G., Miettinen, O.S., Libby, D.M., Pasmantier, M.W., Koizumi, J., Altorki, N.K., others, 1999. Early lung cancer action project: overall design and findings from baseline screening. The Lancet 354, 99–105.

Ilegbusi, O.J., Li, Z., Seyfi, B., Min, Y., Meeks, S., Kupelian, P., Santhanam, A.P., 2012. Modeling airflow using subject-specific 4DCT-based deformable volumetric lung models. Int J Biomed Imaging 2012, 1–10.

Ilegbusi, O.J., Seyfi, B., Salvin, R., 2014. Patient-specific model of lung deformation using spatially dependent constitutive parameters. Math Comput Modell Dyn Syst 20, 546–556.

Kalender, W.A., Kyriakou, Y., 2007. Flat-detector computed tomography (FD-CT). Eur Radiol 17, 2767–2779.

Kay Sun, Pheiffer, T.S., Simpson, A.L., Weis, J.A., Thompson, R.C., Miga, M.I., 2014. Near real-time computer assisted surgery for brain shift correction using biomechanical models. IEEE J Transl Eng Health Med 2, 1–13.

Keating, J., Singhal, S., 2016. Novel methods of intraoperative localization and margin assessment of pulmonary nodules. Semin Thorac Cardiovasc Surg 28, 127–136.

Klein, S., Staring, M., Murphy, K., Viergever, M., Pluim, J., 2010. elastix: A toolbox for intensity-based medical image registration. IEEE Trans Med Imag 29, 196–205.

Kondo, R., Yoshida, K., Hamanaka, K., Hashizume, M., Ushiyama, T., Hyogotani, A., Kurai, M., Kawakami, S., Fukushima, M., Amano, J., 2009. Intraoperative ultrasonographic localization of pulmonary ground-glass opacities. J Thorac Cardiov Sur 138, 837–842.

Lehr, J., 1983. Truncated-view artifacts: clinical importance on CT. Am J Roentgenol 141, 183–191.

Lesage, A.C., Rajaram, R., Tam, A.L., Rigaud, B., Brock, K.K., Rice, D.C., Cazoulat, G., 2020. Preliminary evaluation of biomechanical modeling of lung deflation during minimally invasive surgery using pneumothorax computed tomography scans. Physics in Medicine & Biology 65, 225010.

Levitzky, M.G., 2007. Pulmonary Physiology. McGraw-Hill Professional Publishing, Blacklick, USA.

Li, P., Malsch, U., Bendl, R., 2008. Combination of intensity-based image registration with 3D simulation in radiation therapy. Phys Med Biol 53, 4621–4637.

Maekawa, H., Nakao, M., Mineura, K., Chen-Yoshikawa, T.F., Matsuda, T., 2020. Model-based registration for pneumothorax deformation analysis using intraoperative cone-beam ct images , 5818–5821.

Maintz, J., Viergever, M.A., 1998. A survey of medical image registration. Med Image Anal 2, 1–36.

McClelland, J., Hawkes, D., Schaeffter, T., King, A., 2013. Respiratory motion models: A review. Med Image Anal 17, 19–42.

Mendizabal, A., Márquez-Neila, P., Cotin, S., 2020. Simulation of hyperelastic materials in real-time using deep learning. Medical Image Analysis 59, 101569.

Miga, M.I., Paulsen, K.D., Hoopes, P.J., Kennedy, F.E., Hartov, A., Roberts, D.W., 2000. In vivo modeling of interstitial pressure in the brain under surgical load using finite elements. J Biomech Eng 122, 354–363.

Mohiuddin, K., Haneuse, S., Sofer, T., Gill, R., Jaklitsch, M.T., Colson, Y.L., Wee, J., Bueno, R., Mentzer, S.J., Sugarbaker, D.J., Swanson, S.J., 2014. Relationship between margin distance and local recurrence among patients undergoing wedge resection for small ($\leq$2 cm) non-small cell lung cancer. J Thorac Cardiov Sur 147, 1169–1177.

Morin, F., Courtecuisse, H., Reinertsen, I., Le Lann, F., Palombi, O., Payan, Y., Chabanas, M., 2017. Brain-shift compensation using intraoperative ultrasound and constraint-based biomechanical simulation. Medical Image Analysis 40, 133–153.

Murphy, K., van Ginneken, B., Reinhardt, J.M., Kabus, S., Kai Ding, Xiang Deng, Kunlin Cao, Kaifang Du, Christensen, G.E., Garcia, V., Vercauteren, T., Ayache, N., Commowick, O., Malandain, G., Glocker, B., Paragios, N., Navab, N., Gorbunova, V., Sporring, J., de Bruijne, M., Xiao Han, Heinrich, M.P., Schnabel, J.A., Jenkinson, M., Lorenz, C., Modat, M., McClelland, J.R., Ourselin, S., Muenzing, S.E.A., Viergever, M.A., De Nigris, D., Collins, D.L., Arbel, T., Peroni, M., Rui Li, Sharp, G.C., Schmidt-Richberg, A., Ehrhardt, J., Werner, R., Smeets, D., Loeckx, D., Gang Song, Tustison, N., Avants, B., Gee, J.C., Staring, M., Klein, S., Stoel, B.C., Urschler, M., Werlberger, M., Vandemeulebroucke, J., Rit, S., Sarrut, D., Pluim, J.P.W., 2011. Evaluation of registration methods on thoracic CT: The EMPIRE10 challenge. IEEE Trans Med Imag 30, 1901–1920.

Nakao, M., Tokuno, J., Chen-Yoshikawa, T., Date, H., Matsuda, T., 2019. Surface deformation analysis of collapsed lungs using model-based shape

matching. International Journal of Computer Assisted Radiology and Surgery 14, 1763–1774.

Narasimhan, S., Weis, J.A., González, H.F.J., Thompson, R.C., Miga, M.I., 2018. In vivo modeling of interstitial pressure in a porcine model: approximation of poroelastic properties and effects of enhanced anatomical structure modeling. Journal of Medical Imaging 5, 1.

National Lung Screening Trial Research Team, Aberle, D.R., Adams, A.M., Berg, C.D., Black, W.C., Clapp, J.D., Fagerstrom, R.M., Gareen, I.F., Gatsonis, C., Marcus, P.M., Sicks, J.D., 2011. Reduced lung-cancer mortality with low-dose computed tomographic screening. N Engl J Med 365, 395–409.

Paulsen, K., Miga, M., Kennedy, F., Hoopens, P., Hartov, A., Roberts, D., 1999. A computational model for tracking subsurface tissue deformation during stereotactic neurosurgery. IEEE Trans Biomed Eng 46, 213–225.

Rietzel, E., Chen, G.T.Y., 2006. Deformable registration of 4D computed tomography data. Med Phys 33, 4423–4430.

Rocco, G., Cicalese, M., La Manna, C., La Rocca, A., Martucci, N., Salvi, R., 2011. Ultrasonographic identification of peripheral pulmonary nodules through uniportal video-assisted thoracic surgery. Ann Thorac Surg 92, 1099–1101.

Rouzé, S., de Latour, B., Flécher, E., Guihaire, J., Castro, M., Corre, R., Haigron, P., Verhoye, J.P., 2016. Small pulmonary nodule localization with cone beam computed tomography during video-assisted thoracic surgery: a feasibility study. Interact Cardiov Th 22, 705–711.

Ruan, D., Esedoglu, S., Fessler, J.A., 2009. Discriminative sliding preserving regularization in medical image registration, in: 2009 IEEE International Symposium on Biomedical Imaging: From Nano to Macro, pp. 430–433.

Ruhaak, J., Polzin, T., Heldmann, S., Simpson, I.J.A., Handels, H., Modersitzki, J., Heinrich, M.P., 2017. Estimation of large motion in lung CT by integrating regularized keypoint correspondences into dense deformable registration. IEEE Trans Med Imag 36, 1746–1757.

Samavati, N., Velec, M., Brock, K., 2015. A hybrid biomechanical intensity based deformable image registration of lung 4DCT. Phys Med Biol 60, 3359–3373.

Schmidt-Richberg, A., Werner, R., Handels, H., Ehrhardt, J., 2012. Estimation of slipping organ motion by registration with direction-dependent regularization. Med Image Anal 16, 150–159.

Schulze, R., Heil, U., Gross, D., Bruellmann, D., Dranischnikow, E., Schwanecke, U., Schoemer, E., 2011. Artefacts in CBCT: a review. Dentomaxillofac Rad 40, 265–273.

Seyfi Noferest, B., Santhanam, A.P., Ilegbusi, O.J., 2018. Effect of gravity on subject-specific human lung deformation. Math Comput Modell Dyn Syst 24, 87–101.

Sotiras, A., Davatzikos, C., Paragios, N., 2012. Deformable Medical Image Registration: A Survey. resreport RR-7919. INRIA.

Suzuki, K., Nagai, K., Yoshida, J., Ohmatsu, H., Takahashi, K., Nishimura, M., Nishiwaki, Y., 1999. Video-assisted thoracoscopic surgery for small indeterminate pulmonary nodules. Chest 115, 563–568.

Tehrani, J.N., Yang, Y., Werner, R., Lu, W., Low, D., Guo, X., Wang, J., 2015. Sensitivity of tumor motion simulation accuracy to lung biomechanical modeling approaches and parameters. Phys Med Biol 60, 8833–8849.

Uneri, A., Nithiananthan, S., Schafer, S., Otake, Y., Stayman, J.W., Kleinszig, G., Sussman, M.S., Prince, J.L., Siewerdsen, J.H., 2013. Deformable registration of the inflated and deflated lung in cone-beam CT-guided thoracic surgery: Initial investigation of a combined model- and image-driven approach. Med Phys 40, 017501.

Verruijt, A., 2013. Theory and problems of poroelasticity. Delft University of Technology.

Wada, H., Anayama, T., Hirohashi, K., Nakajima, T., Kato, T., Waddell, T.K., Keshavjee, S., Yoshino, I., Yasufuku, K., 2016. Thoracoscopic ultrasonography for localization of subcentimetre lung nodules. Eur J Cardio-Thorac 49, 690–697.

Werner, R., Ehrhardt, J., Schmidt, R., Handels, H., 2009. Patient-specific finite element modeling of respiratory lung motion using 4D CT image data. Med Phys 36, 1500–1511.

Wolf, A.S., Swanson, S.J., Yip, R., Liu, B., Tarras, E.S., Yankelevitz, D.F., Henschke, C.I., Taioli, E., Flores, R.M., 2017. The impact of margins on outcomes after wedge resection for stage i non-small cell lung cancer. Ann Thorac Surg. 104, 1171–1178.

Wu, Z., Rietzel, E., Boldea, V., Sarrut, D., Sharp, G.C., 2008. Evaluation of deformable registration of patient lung 4DCT with subanatomical region segmentations. Med Phys 35, 775–781.

Yang, S.M., Ko, W.C., Lin, M.W., Hsu, H.H., Chan, C.Y., Wu, I.H., Chang, Y.C., Chen, J.S., 2016. Image-guided thoracoscopic surgery with dye localization in a hybrid operating room. J Thorac Dis 8, S681–S689.

Yongchoel Choi, Seungyong Lee, 1999. Local injectivity conditions of 2D and 3D uniform cubic B-spline functions, in: Proceedings. Seventh Pacific Conference on Computer Graphics and Applications, Seoul, South Korea. pp. 302–311.

Zhang, T., Orton, N.P., Mackie, T.R., Paliwal, B.R., 2004. Technical note: A novel boundary condition using contact elements for finite element based deformable image registration. Med Phys 31, 2412–2415.

Zhao, Z.R., Lau, R.W.H., Yu, P.S.Y., Wong, R.H.L., Ng, C.S.H., 2016. Image-guided localization of small lung nodules in video-assisted thoracic surgery. J Thorac Dis 8, S731–S737.